Cell Stem Cell

Article

Enhanced viability and functional maturity of iPSC-derived islet organoids by collagen-VI-enriched ECM scaffolds

Graphical abstract

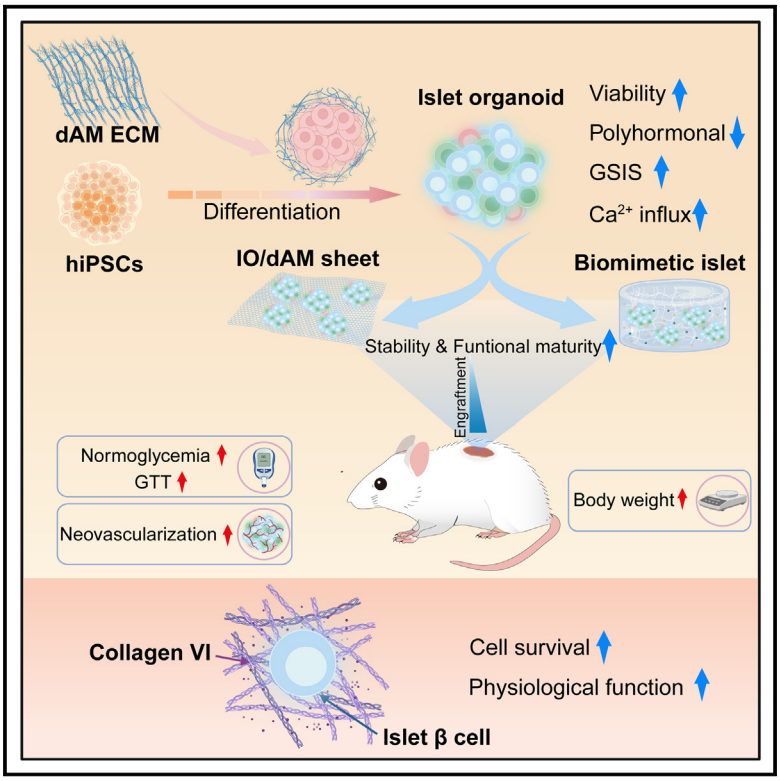

Highlights

- dAM ECM hydrogel promotes the maturation and function of human islet organoids
- dAM sheet supports engraftment of islet organoids
- Col VI enhances islet organoid viability and function
- Col VI is critical for biomimetic islets' architectural and physiological properties

Authors

Deliang Zhu, Zixin Chen, Kaimin Guo, ..., Qizheng Mou, Zhongjun Zhou, Guoxiang Jin

Correspondence

zhongjun@hku.hk (Z.Z.), gxjinking@163.com (G.J.)

In brief

Jin and colleagues demonstrate that dAM ECM hydrogel promotes islet organoid development and sustains viability. The dAM sheet enhances hiPSC-islet organoid engraftment and rapidly reverses diabetes. The Col-VI-enriched ECM scaffold is able to support the key features of islet organoids. These findings offer insights for improved biomimetic islet organoids in diabetes treatment.

Zhu et al., 2025, Cell Stem Cell *32*, 547–563
April 3, 2025
https://doi.org/10.1016/j.stem.2025.02.001

CellPress

Cell Stem Cell

CellPress

Article

Enhanced viability and functional maturity of iPSC-derived islet organoids by collagen-VI-enriched ECM scaffolds

Deliang Zhu,[1,2] Zixin Chen,[1,2] Kaimin Guo,[3] Qingqiang Xie,[1] Yuxiu Zou,[1] Qizheng Mou,[4] Zhongjun Zhou,[4,*] and Guoxiang Jin[1,2,5,*]

[1]Guangdong Cardiovascular Institute, Medical Research Institute, School of Basic Medical Science, Guangdong Provincial People's Hospital (Guangdong Academy of Medical Sciences), Southern Medical University, Guangzhou 510080, China

[2]Guangdong Provincial Geriatrics Institute, Guangdong Provincial People's Hospital, Guangdong Academy of Medical Sciences, Guangzhou 510080, China

[3]Department of Obstetrics and Gynecology, Guangzhou Women and Children's Medical Center, Guangzhou Medical University, Guangzhou 510627, China

[4]School of Biomedical Sciences, The University of Hong Kong, Hong Kong, China

[5]Lead contact

*Correspondence: zhongjun@hku.hk (Z.Z.), gxjinking@163.com (G.J.)

https://doi.org/10.1016/j.stem.2025.02.001

SUMMARY

Islet organoids derived from pluripotent stem cells offer a promising solution for the shortage of cadaveric donors in diabetes treatment. However, challenges remain in improving their differentiation, viability, functional maturity, and engraftment. Here, we generated improved islet organoids with high viability and functionality by employing extracellular matrix (ECM) hydrogel of decellularized amniotic membrane (dAM). The dAM sheet facilitates islet organoid engraftment and rapidly restores normoglycemia in diabetic mice, accompanied by increased body weight and augmented insulin release in response to glucose. Interestingly, collagen VI (Col VI) was identified as a key component of islet niche, enhancing islet cell viability and biological function. Col-VI-based biomimetic ECM recapitulates the native environment and exhibits superior physiological properties. Importantly, the cellular composition and endocrine function of optimized induced pluripotent stem cell (iPSC)-derived islet organoids are comparable with those of human islets. Our findings offer a valuable platform for future endeavors in organoid-transplantation-based therapy of diabetes.

INTRODUCTION

Diabetes mellitus is an epidemic metabolic disease that affects more than 460 million people worldwide.[1] The prevalence increases due to changes in lifestyle and diet.[2] Cadaveric islet transplantation could effectively maintain glucose homeostasis.[3] However, the widespread use of this therapeutic technology is limited by the scarcity of suitable donors and continuous immunosuppression. The most promising approach is the generation of pluripotent stem cell (PSC)-derived islet organoids (IOs), which provide an unlimited source to overcome these obstacles in diabetes treatment.

Currently, there are numerous protocols available for generating pancreatic β cells or IOs from PSCs using stepwise differentiation based on pancreatic development.[4–6] Accumulated studies have reported the benefits of decellularized matrices derived from rat pancreas, kidney, lung, and small intestine in promoting islet development and enhancing the function of islets.[7–10] Amniotic membrane (AM) is the innermost layer of the fetal placenta. Its unique structural physical and biological properties make it a versatile biological membrane that is widely used in tissue engineering and regenerative medicine.[11] However, little has been done to explore their potential function in the generation of IOs,[12,13] as well as their effects on the development, survival, engraftment, and function of IOs, especially in terms of clinical settings.

Specific microenvironmental niches, including biochemical cues and mechanical signals, are intriguing candidate components in the extracellular matrix (ECM) to influence the survival and sustained insulin (INS) secretion of IOs. A recent study found that the combination of collagen (Col) IV, nidogen, and laminin in the peri-islet ECM enhanced glucose-stimulated insulin secretion (GSIS) in pancreatic islets.[14] The evidence of cell-ECM interactions critical for islet viability and function also comes from 3D-printed IOs constructed with the combination of pancreatic ECM and hyaluronic acid methacrylate hydrogel.[15] Accumulated evidence suggests that IOs with ECM scaffold can not only evade immune cell detection but also facilitate angiogenesis.[15,16] These findings underscore the potential of engineered ECM in enhancing the therapeutic efficacy of IOs.

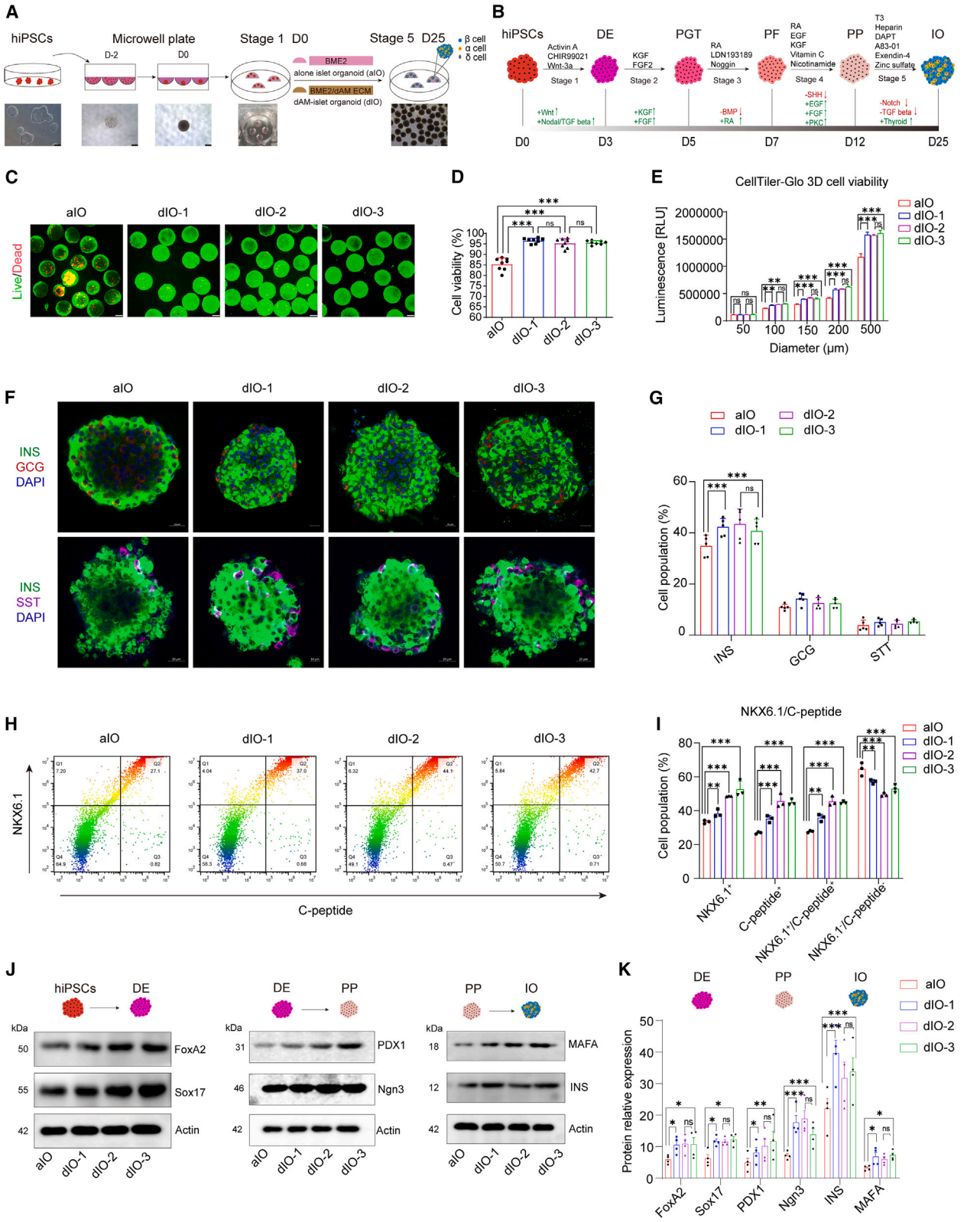

(legend on next page)

In this study, we developed an approach by applying dAM ECM hydrogel to generate IOs from human induced PSCs (hiPSCs) with high viability and functionality. The hiPSC-IOs were seeded on dAM sheet, resulting in efficient IOs engraftment. In particular, we identified that Col VI played an important role in facilitating the viability and functionality of IOs. Furthermore, we validated that the cellular composition, endocrine functions, and *in vivo* diabetes reversal of optimized hiPSC-IOs closely resembled those of human islets.

RESULTS

Generation of high viability IOs derived from hiPSCs by dAM ECM hydrogel

To generate productive and uniform IOs, we developed a strategy to differentiate hiPSCs into IOs by utilizing optimized dAM ECM hydrogel and microwell aggregation. This procedure, as depicted in Figure 1A, spanned a period of 27 days and involved the utilization of an embedded technology combining round-bottom ultralow attachment 96-well plate along with basement membrane extract (BME)2/dAM ECM hydrogel. The undifferentiated hiPSCs characterized by the expression of key stem cell markers and a normal karyotype (Figures S1A–S1C) were seeded in the 96-microwell plate, which facilitated efficient and homogeneous aggregation of hiPSCs in a solid 3D clonal cell cluster. An increased number of seeded cells were correlated with an enlarged 3D cell cluster, accompanied by decreased viability (Figures S1D–S1H). The systematic workflow involved treatments with growth factors and various agonists or antagonists of different signaling pathways to allow the gradual differentiation of iPSC in the aggregated cell cluster into definitive endoderm (DE), primitive gut tube (PGT), posterior foregut (PF), pancreatic progenitor (PP), and, finally, IOs. This protocol included sequential culture steps using factors that affect signaling pathways, such as wingless-type MMTV integration site family (WNT), activin A, epidermal growth factor (EGF), transforming growth factor β (TGF-β), thyroid hormone, retinoic acid, and Notch (Figure 1B).

Numerous differentiated cells are vulnerable during the long-term differentiation process, particularly in the absence of ECM support. The AM's unique structure and properties make it an ideal candidate for tissue engineering and regenerative medicine (Figure S1I). We speculated that dAM ECM hydrogel could improve the viability of hiPSCs differentiation into IOs. To test this hypothesis, we collected human AM, followed by decellularization. The dAM was then prepared as hydrogel for hiPSCs differentiation (Figures S1J and S1K). Treatment of AM with SDS-Triton X-100 buffer facilitated cell removal and significantly reduced residual DNA content, compared with the native AM (Figure S1L). IO differentiation was performed in 10, 20, 30 μg/mL dAM ECM hydrogel or alone with BME2 hydrogel, henceforth called dIO-1, dIO-2, dIO-3, and aIO, respectively. Compared with the aIO, cell viability and total cellular adenosine triphosphate (ATP) content levels were significantly higher in hiPSC-IOs cultured on dAM hydrogel (Figures 1C–1E). Western blotting showed that Bcl2 was significantly increased, while Bax decreased in the dIO-1, dIO-2, and dIO-3 groups (Figure S2A), in comparison with the aIO group. Collectively, these data suggested that we have established a protocol for generating robustly productive and highly viable homogeneous IOs.

dAM ECM hydrogel promotes hiPSCs differentiation to IOs and improves its functional maturity

To examine the impact of dAM ECM hydrogel on differentiation of hiPSCs into IOs, immunofluorescence staining was performed for α cell (glucagon [GCG]), β cell (INS), and δ cell (somatostatin [SST]) markers on the sections of the IOs. Notably, the dIO-1, dIO-2, and dIO-3 groups showed enhanced INS expression (Figures 1F and 1G). Additionally, the C-peptide and NKX6.1 double-positive populations were higher in the differentiated clusters from dIO-1, dIO-2, and dIO-3, compared with those in the aIO groups, indicating that dAM ECM hydrogel enhances hiPSCs differentiation into β cells (Figures 1H, 1I, S2B, and S2C). Furthermore, in comparison with the aIO group, the dIO-1, dIO-2, and dIO-3 groups exhibited enhanced expression of DE markers FoxA2 and Sox17, PP markers Ngn3 and PDX1, and mature markers INS and MAF bZIP transcription factor A (MAFA) at the final stage (Figures 1J and 1K). These findings suggest that dAM ECM hydrogel at 10 μg/mL is sufficient to promote IO development.

Immature IOs derived from hiPSCs display a polyhormonal state and lack GSIS function. A significant increase in the proportion of monohormonal cells, particularly INS^+GCG^- β cells, was found in the presence of dAM ECM hydrogel. In contrast, the aIO group exhibited a higher percentage of INS^+GCG^+ polyhormonal

Figure 1. dAM ECM hydrogel improves IO viability and promotes islet development

(A) Flow chart (top) and representative phase-contrast images (bottom) of the strategy of IO generation. Scale bars, 250 μm.

(B) Schematic representation of the stepwise differentiation protocol of IOs derived from hiPSCs. The up and down arrows indicate agonists and inhibitors, respectively.

(C) Images of live and dead cells of aIO, dIO-1, dIO-2, and dIO-3 stained with calcein AM (green)/propidium iodide (PI) (red). Scale bars, 100 μm.

(D) Quantity of cell viability across IO types aIO, dIO-1, dIO-2, and dIO-3. Data are represented as mean ± SEM. One-way ANOVA with Dunnett's multiple comparison test. $n = 8$. $^{***}p < 0.001$.

(E) ATP content levels of aIO, dIO-1, dIO-2, and dIO-3 with various diameters. Data are represented as mean ± SEM. Two-way ANOVA. $n = 3$. $^{**}p < 0.01$, $^{***}p < 0.001$.

(F) Representative immunostaining for INS, GCG, and SST in aIO, dIO-1, dIO-2, and dIO-3. Nuclei were counterstained with DAPI. Scale bars, 20 μm.

(G) Quantitative analysis of INS, GCG, and SST positive cells in aIO, dIO-1, dIO-2, and dIO-3. Data presented as mean ± SEM. Two-way ANOVA. $n = 5$. $^{***}p < 0.001$.

(H) Representative flow cytometry dot plots of C-peptide and NKX6.1 at the final stage.

(I) Quantitative analysis of the fraction of C-peptide and NKX6.1 positive cells in aIO, dIO-1, dIO-2, and dIO-3. Data are represented as mean ± SEM. One-way ANOVA. $n = 3$. $^{**}p < 0.01$, $^{***}p < 0.001$.

(J) Representative western blots of FoxA2 and Sox17 for endoderm, PDX1 and Ngn3 for PP cells, and INS and MAFA for mature pancreatic β cells.

(K) Statistical analysis of western blot data in (J). Data are represented as mean ± SEM. One-way ANOVA. $n = 3$. $^{*}p < 0.05$, $^{**}p < 0.01$, $^{***}p < 0.001$.

See also Figures S1 and S2.

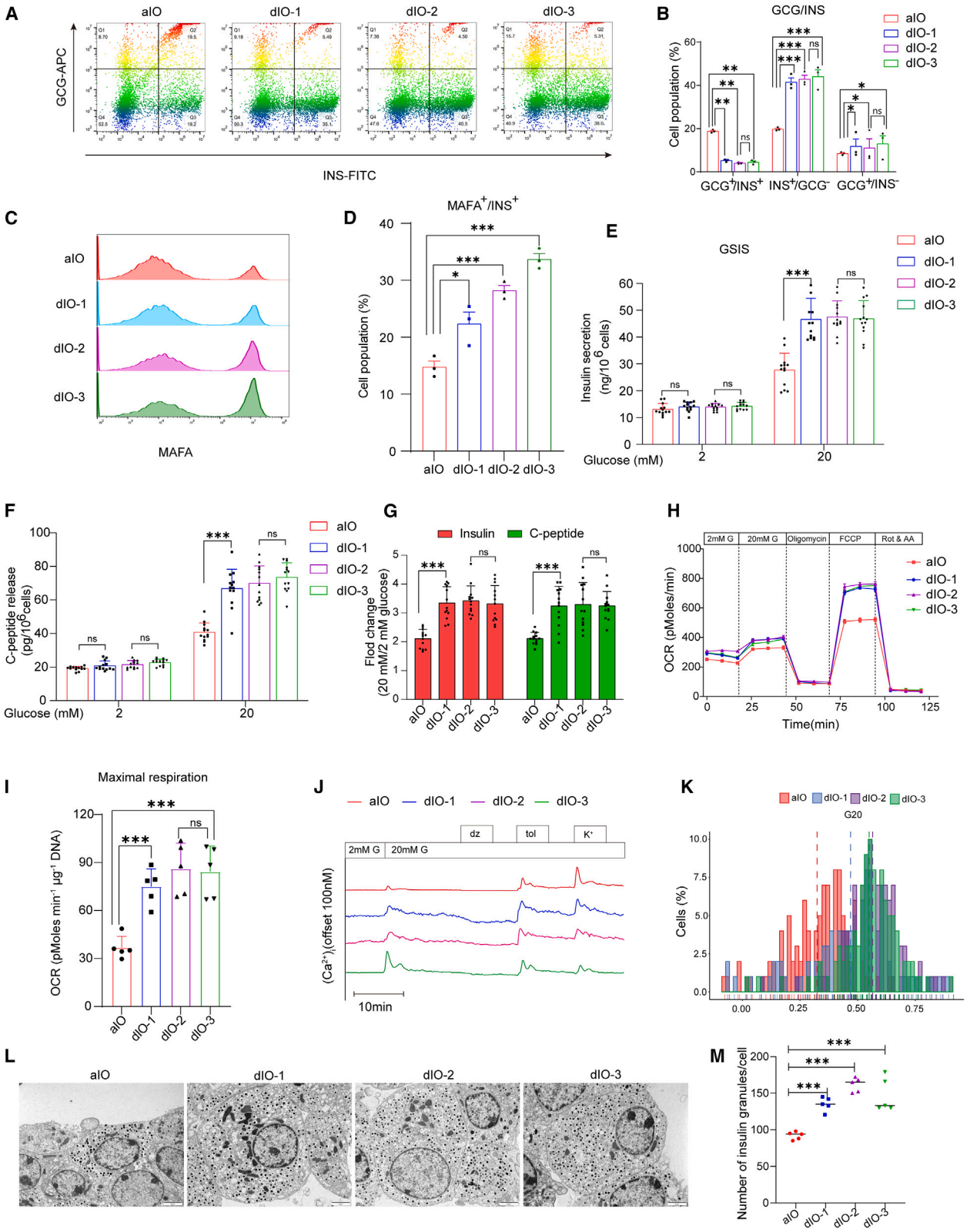

(legend on next page)

cells (Figures 2A and 2B). As expected, a robust expression of the mature marker MAFA was observed in the dIO-1, dIO-2, and dIO-3 groups. A minor population co-expressed MAFA and INS in the aIO group, while an increased population of MAFA and INS double-positive cells was observed in the dIO-1, dIO-2, and dIO-3 groups (Figures 2C, 2D, S2D, and S2E). The findings suggested that dAM hydrogel results in increased subpopulation of mature β cells in hiPSC-derived IOs.

To evaluate the physiological function of β cells, INS and C-peptide release in response to glucose challenge were measured. Compared with the aIO group, the amount of INS and C-peptide released in response to 20 mM glucose was significantly higher in the dIO-1, dIO-2, and dIO-3 groups, suggesting stronger GSIS (Figures 2E–2G). We then examined the oxygen consumption rate (OCR) as metabolism is an important parameter for proper function of β cells. Cells from the aIO, dIO-1, dIO-2, and dIO-3 groups exhibited increased OCR upon stimulation with high glucose. When normalized to DNA content, the maximal respiration OCR in the dIO-1, dIO-2, and dIO-3 groups was significantly higher than that observed in the aIO group (Figures 2H and 2I). To further evaluate the function of β cells in hiPSC-derived IOs, we measured the cytoplasmic Ca^{2+} concentration ($[Ca^{2+}]_i$) oscillations within β cells. Elevated glucose levels caused an influx of calcium ions that trigger INS exocytosis in β cells. Cells from the dIO-1, dIO-2, and dIO-3 groups demonstrated increased $[Ca^{2+}]_i$ levels in response to high glucose stimulation compared with those from the aIO group. These oscillations were diminished upon the opening of K_{ATP} channels with diazoxide and were enhanced upon their closure with tolbutamide (Figures 2J and 2K). Subsequently, the INS granules in β cells were examined by transmission electron microscopy (TEM). The average number of INS granules per cell in the dIO groups was significantly more than that in the aIO group (Figures 2L and 2M). Taken together, these data suggested that dAM ECM hydrogel facilitates the functional maturation of hiPSC-derived IOs.

dAM sheet maintains IO functional integrity

To overcome the obstacles in the transplantation of hiPSC-derived IOs and improve the stability of IOs, we developed a dAM sheet that could offer both architecture and physical support for the organoids. H&E and scanning electron microscopy (SEM) revealed that the dAM lost the majority of cellular components after decellularization while retaining the ECM components (Figure 3A). To evaluate the effect of the dAM sheet, we compared the properties of the IOs among different groups, including aIO, dIO, aIO cultured on a dAM sheet (aIO/dAM sheet), and dIO cultured on a dAM sheet (dIO/dAM sheet) (Figure S3A). The dAM, as revealed by SEM and TEM analysis, showed an ultrastructure favorable for cell attachment (Figure 3A). As anticipated, the IOs examined by SEM anchored well to the dAM sheet and maintained good morphology (Figure 3B). The percentage of apoptotic cells in IOs on the dAM sheet was greatly reduced (Figures 3C and 3D). Western blotting showed a decrease in the apoptosis-associated marker Bax, while levels of Bcl2 and E-cadherin were significantly elevated (Figures 3E and 3F). Importantly, IOs residing on the dAM sheet not only retained their ability to secrete INS but also exhibited an enhanced response to glucose challenge (Figures 3G and 3H). Interestingly, IOs cultured on the dAM sheet exhibited minimal cell death when exposed to hypoxia, a condition leading to significant cell death in the IOs in the absence of dAM (Figures 3I and 3J). The dAM ECM hydrogel and dAM sheet were effective in reducing the markers SCL18A1, DDC, TPH1, and FEV of enterochromaffin (EC) cells—a subtype of enteroendocrine cells—in hiPSC-derived IOs, which are undesired byproducts of islet differentiation (Figures S3B–S3G). Additionally, the dAM sheet slightly mitigated the immune response in C57BL6J mice following the transplantation of hiPSC-derived IOs (Figures S3H and S3I).

Cryopreservation represents another potential challenge in the application of IOs. Interestingly, cryopreservation of IOs for a duration of 1 month did not result in a significant death of cells in the aIO/dAM sheet groups compared with that in the aIO groups (Figures 3K and 3L). Recovered IOs cultured in aIO/dAM sheet exhibited increased INS secretion function and were capable of restoring normoglycemia in a mouse model of diabetes (Figures S4A–S4D). This implied that the aIO/dAM sheet has the potential to maintain the viability and physiological function of IOs both *in vitro* and *in vivo*, even immediately after thawing. This facilitates the pooling, long-term banking,

Figure 2. dAM ECM hydrogel enhances hiPSC-derived IO functional maturation

(A) Representative flow cytometry profiles of α and β cell-specific markers at the final stage.

(B) Quantification of the proportion of INS^+/GCG^+, INS^+/GCG^-, and INS^-/GCG^+ cells across experimental groups: aIO, dIO-1, dIO-2, and dIO-3. Data are represented as mean ± SEM. One-way ANOVA. $n = 3$. $^*p < 0.05$, $^{**}p < 0.01$, $^{***}p < 0.001$.

(C) Representative flow cytometry histograms of MAFA in the aIO, dIO-1, dIO-2, and dIO-3 groups.

(D) Quantification analysis of the proportion of $INS^+/MAFA^+$ cells in the aIO, dIO-1, dIO-2, and dIO-3 groups. Data are represented as mean ± SEM. One-way ANOVA. $n = 3$. $^*p < 0.05$, $^{***}p < 0.001$.

(E) GSIS function assay for aIO, dIO-1, dIO-2, and dIO-3. Data are represented as mean ± SEM. Two-way ANOVA. $n = 13$. $^{***}p < 0.001$.

(F) Measurements of human C-peptide secreted by aIO dIO-1, dIO-2, and dIO-3 upon sequential glucose challenges at 2 and 20 mM glucose. Data are represented as mean ± SEM. Two-way ANOVA. $n = 13$. $^{***}p < 0.001$.

(G) INS and C-peptide fold change in aIO, dIO-1, dIO-2, and dIO-3 stimulated with 2, 20 mM glucose. Data are represented as mean ± SEM. One-way ANOVA. $n = 13$. $^{***}p < 0.001$.

(H) Representative OCR curve of aIO, dIO-1, dIO-2, and dIO-3.

(I) Maximal respiratory consumption rates in aIO, dIO-1, dIO-2, and dIO-3. Data are represented as mean ± SEM. One-way ANOVA. $n = 5$. $^{***}p < 0.001$.

(J) Representative $[Ca^{2+}]_i$ recordings from aIO, dIO-1, dIO-2, and dIO-3 during exposure to 2 and 20 mM glucose, 250 μM diazoxide, 1 mM tolbutamide, and 30 mM K^+.

(K) Histograms illustrating the $[Ca^{2+}]_i$ change in response to 20 mM glucose, normalized to levels at 2 mM glucose in cells from aIO, dIO-1, dIO-2, and dIO-3.

(L) TEM electron micrograph displaying granules within sectioned cells of aIO, dIO-1, dIO-2, and dIO-3. Scale bar, 2 μm.

(M) Quantification of the granules in the aIO, dIO-1, dIO-2, and dIO-3 groups. Data are represented as mean ± SEM. One-way ANOVA. $n = 5$. $^{***}p < 0.001$.

See also Figure S2.

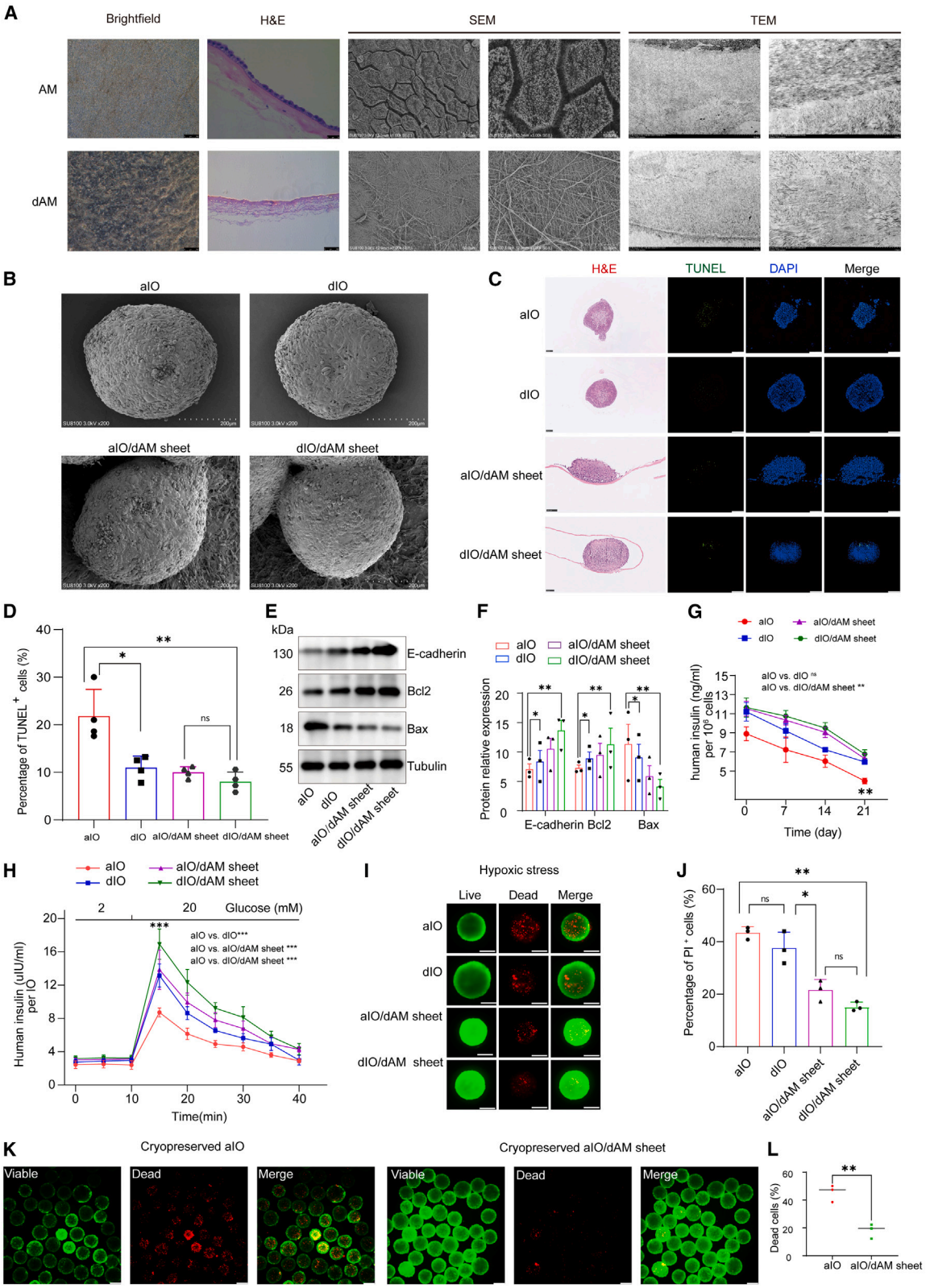

Figure 3. dAM sheet exhibits high biocompatibility to accommodate and maintain islet functional integrity

(A) Characterization of AM and decellularized AM (dAM) through gross morphology, hematoxylin and eosin (H&E) staining, and ultrastructural assessment.

(B) SEM images of aIO, dIO, aIO, or dIO resident on the dAM sheet. Scale bar, 20 μm.

(legend continued on next page)

transportation, and immediate transplantation without subculture upon the arrival of the frozen IOs.

dAM ECM hydrogel and dAM sheet improve the function of IOs *in vivo* and ameliorate diabetes in mice

We then evaluated the functionality of hiPSC-IOs in diabetic hyperglycemia by transplantation into the dorsal subcutaneous region of streptozotocin (STZ)-induced diabetic immune-compromised mice. H&E staining and INS immunofluorescence staining confirmed the successful destruction of mouse islet cells by STZ (Figure S4A). Healthy un-transplanted (normal) and STZ-induced un-transplanted (STZ-no TX) mice served as additional controls. The mice were monitored weekly for changes in blood glucose levels and body weight. Additionally, intraperitoneal glucose tolerance tests (IPGTT) and INS levels in serum were measured at 1 and 3 months post-transplantation (Figures 4A and 4B). Transplantation study results showed that the STZ-no TX group mice remained hyperglycemic until the endpoint and showed progressive loss of body weight. In contrast, recipients of the dIO/dAM sheet showed rapid restoration of blood glucose levels and an increase in body weight, compared with recipients of the aIO, dIO, and aIO/dAM sheet groups (Figures 4C and 4D). The dIO/dAM sheet group of diabetic mice exhibited the highest efficacy of normoglycemia among all the recipient groups. In contrast, the aIO group exhibited the lowest efficacy (Figure 4E). There were no significant differences in glucose levels and body weight between the dIO/dAM sheet-transplanted group and the healthy normal group up to 3 months post-transplantation. Similar to the dIO/dAM sheet recipients, the recipients of dIO and aIO/dAM sheet also exhibited a slight decrease in blood glucose levels compared with those receiving aIO. To further assess the impact of various IOs on glycemic control, the IPGTT was performed in diabetic mice at 1 and 3 months post-transplantation. The glucose response curve in the recipients of the dIO/dAM sheet was similar to that of normal mice, and their blood glucose returned to normal levels faster than in recipients of aIO, dIO, or aIO/dAM sheet (Figure 4F). To determine whether human INS secreted from IOs regulates glycemia in diabetic mice, human C-peptide was detected by ELISA in the blood. The serum levels of human C-peptide were higher in recipients of the dIO/dAM sheet than in recipients of aIO, dIO, and aIO/dAM upon either fasting or glucose injection stimulation at 1 and 3 months post-transplantation, confirming the function of xenografts (Figure 4G). The removal of the engrafted organoids resulted in a sharp increase in blood glucose levels, confirming the role of engrafted hiPSC-derived IOs in glycemia control in diabetic mice (Figure 4H). These findings suggest that dAM hydrogel and dAM sheet support the functionality of IOs and accelerate the restoration of blood glucose levels in diabetic mice.

dAM sheet preserves survival and drives neovascularization in the grafts

To track the cell survival of engrafted IOs, we transduced the organoid cells to express luciferase. Bioluminescence imaging (BLI) revealed a localized signal in the engrafted subcutaneous region. The dIO/dAM sheet group exhibited a stronger intensity compared with the aIO, dIO, and aIO/dAM sheet groups at both 1 and 3 months post-transplantation. Interestingly, a significant increase in BLI signal was detected in both the aIO/dAM and dIO/dAM sheet recipients (Figures 4I and 4J). These results suggested that the dAM sheet promotes the survival of transplanted islet cells. To better understand the impact of dAM on IO, animals were sacrificed at 3 months after transplantation, and engrafted IOs were retrieved for histological analysis. The number of dead cells in the engrafts was significantly reduced in the dIO/dAM sheet group, as well as in the dIO and aIO/dAM sheet groups, compared with that in the aIO group (Figures 4K and 4L). Human nuclear antigen (HNA) and C-peptide double-positive staining in the xenografts indicated the survival and INS secretion function in the engrafted IOs (Figure 4M). Grafts from the dIO/dAM sheet group exhibited the highest number of NKX6.1 and C-peptide double-positive cells, with both dIO and aIO/dAM sheet groups showing a notable increase compared with the aIO group. Conversely, grafts of the dIO, aIO/dAM sheet, and dIO/dAM sheet group displayed significantly fewer C-peptide and GCG double-positive cells than those from the aIO group (Figures S5A–S5C). Significantly elevated blood vessel density characterized by enhanced CD31 staining was observed in the dIO, aIO/dAM sheet, and dIO/dAM sheet groups, supporting the promotion of neovascularization (Figures 4N and S5D). Taken together, the dAM sheet enhanced the efficacy of hiPSC-derived IO transplantation by preserving cell survival and facilitating neovascularization.

Col VI improves the survival and function of IOs

To understand the potential mechanism underlying the enhanced efficacy of IOs engraftment by dAM sheet, a mass spectrometry analysis was performed to characterize the ECM composition in dAM and decellularized pancreatic ECM (dpECM). The proteomic analysis identified over 1,400 proteins

(C) Representative H&E staining and terminal deoxynucleotidyl transferase mediated dUTP nick end-labeling (TUNEL) assay images in aIO, dIO, aIO/dAM sheet, and dIO/dAM sheet. Scale bar, 100 μm.
(D) Quantitation of TUNEL-positive nuclei percentages. Data are represented as mean ± SEM. One-way ANOVA. $n = 4$. $^{*}p < 0.05$, $^{**}p < 0.01$.
(E) Western blot analysis of Bax, Bcl2, and E-cadherin in aIO, dIO, aIO/dAM sheet, and dIO/dAM sheet.
(F) Quantitative assessment of protein levels from (E). Data are represented as mean ± SEM. One-way ANOVA. $n = 3$. $^{*}p < 0.05$, $^{**}p < 0.01$.
(G) ELISA quantitation of INS release from aIO, dIO, aIO/dAM sheet, and dIO/dAM sheet. Data are represented as mean ± SEM. Two-way ANOVA. $n = 4$. $^{**}p < 0.01$.
(H) GSIS assay results for aIO, dIO, aIO/dAM sheet, and dIO/dAM sheet. Two-way ANOVA. $n = 10$, $^{***}p < 0.001$.
(I) Live/dead staining of aIO, dIO, aIO/dAM sheet, and dIO/dAM sheet under hypoxic stress. Scale bar, 100 μm.
(J) Cell death quantification in aIO, dIO, aIO/dAM sheet, and dIO/dAM sheet under hypoxic stress. Data are represented as mean ± SEM. One-way ANOVA. $n = 3$. $^{*}p < 0.05$, $^{**}p < 0.01$.
(K) Live/dead staining of recovered aIO and aIO/dAM from cryopreservation. Scale bar, 100 μm.
(L) Cell death quantification in recovered aIO and aIO/dAM from cryopreservation. Data are represented as mean ± SEM, unpaired Student's t test, $^{**}p < 0.01$.
See also Figures S3 and S4.

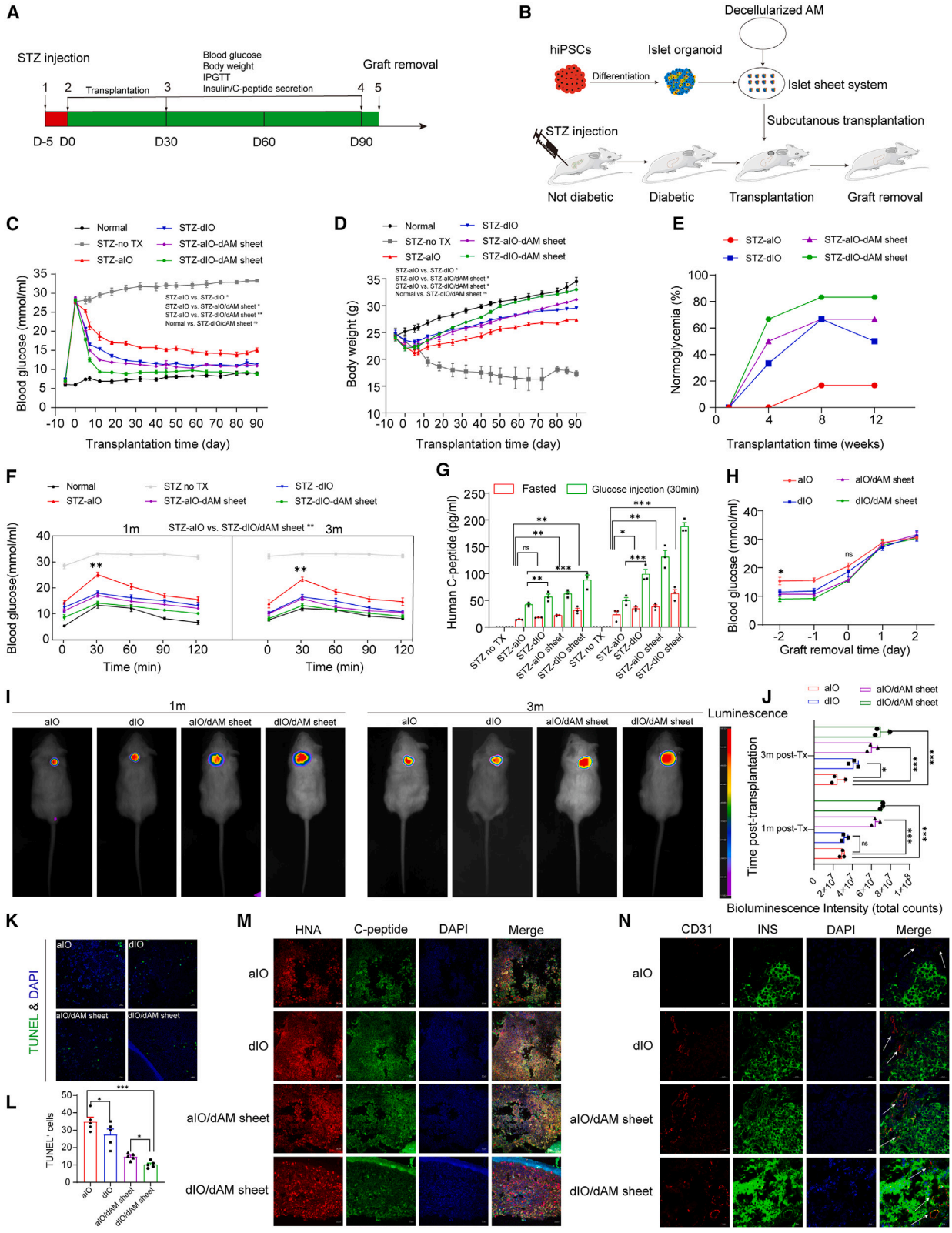

Figure 4. dAM sheet supports IO engraftment to effectively reverse STZ-induced diabetes in NOD/SCID mice

(A) Illustrated timeline of experimental design for *in vivo* studies, including time points of diabetes induction, IOs transplantation, INS/C-peptide measurement, IPGTT, and graft retrieval.

(legend continued on next page)

in dAM and more than 1,900 proteins in dpECM. While the majority of the identified proteins in either dAM or dpECM accounted for less than 5% of the total protein contents, multiple Cols were found to be the most abundant proteins (Figure 5A). Notably, among the 675 common proteins found between dAM and dpECM, only 8 proteins were identified out of the top 50 most abundant proteins in both dAM and dpECM, including Col6A1, Col6A2, FBN1, HSPG2, ColA1, ColA2, Col5A1, and Col5A2 (Figure 5B). The main components of dAM ECM and BME2 hydrogels are listed in Table S1. Immunostaining analysis confirmed the presence of Col VI along with other classic basement membrane proteins (Col IV and laminin) in both mouse pancreas and AM (Figures 5C and 5D). Based on these observations, we speculated that Col VI may play a crucial role in islet viability and function.

To investigate the impact of Col VI on islet viability and functionality, we coated the hiPSC-IOs with Col VI. Significant higher cell viability was observed in the IO cultured with Col VI, particularly during prolonged culture (Figures 5E and 5F). The culture of IO with Col VI was found to significantly enhance cell migration, as well as increase ATP content levels (Figures S6A–S6C). C-peptide secretion in response to high glucose was significantly enhanced in IO-Col VI compared with IO alone, while the response to low glucose was only slightly increased (Figure 5G). Cells from IO-Col VI demonstrated significantly higher cytoplasmic $[Ca^{2+}]_i$ oscillations in response to glucose stimulation compared with cells from IO alone (Figure 5H). Furthermore, reduced cell toxicity in response to glucolipotoxicity was found in IOs when cultured in the presence of Col VI (Figures 5I and 5J). Western blotting analysis revealed a significant increase in the anti-apoptotic protein Bcl2 in the presence of Col VI (Figure S6D). Additionally, immunofluorescence staining showed elevated expressions in INS and Glut1 in IO-Col VI. Elevated INS in the IO-Col VI was confirmed by western blotting (Figures S6E and S6F). These results suggest that Col VI is capable and sufficient to preserve the viability of islet cells and promote the functionality of IO.

To investigate the role of Col VI in IOs, we performed functional annotation, which revealed two key signaling pathways: phosphatidylinositol 3-kinase (PI3K)/serine/threonine kinase (AKT) and focal adhesion (Figure 5K). Further validation of the impact of Col VI on PI3K/AKT signaling in IOs confirmed that treatment with Col VI significantly increased PI3K/AKT phosphorylation (Figure 5L). The expression of E-cadherin in IOs was also elevated when cultured with Col VI, corroborating the role of Col VI in promoting islet cell adhesion (Figure 5M). Interestingly, blocking Col VI receptor $\alpha2\beta1$ led to decreased AKT phosphorylation, indicating that Col VI promotes IO survival and functions via integrin $\alpha2\beta1$, which triggers the PI3K/AKT pathway, ultimately reducing cell death (Figures S6G and S6H). Collectively, these data suggest that Col VI plays a crucial role in preserving the viability and functionality of IOs.

Col VI enables biomimetic islets to maintain high viability and functionality both *in vitro* and *in vivo*

Inadequate ECM in IOs hampers the attainment of mature islet architecture and functional physiology. To obtain functional hiPSC-IOs, we constructed a biomimetic ECM hydrogel to mimic a native microenvironment required for the maintenance of functional IOs. Based on pancreas matrix composition and our own proteomic analysis, we generated two types of ECM scaffold: the first consisted of Col I, laminin, and Col IV (bIO), whereas the second comprised Col I, laminin, Col IV, and Col VI (bIO-Col VI) (Figure 6A). IO without ECM served as a control. Though the fabricated ECM scaffolds exhibited a lower Young's modulus than that of AM, both exhibited mechanical properties favorable for the maintenance of the basic architecture and morphology of the ECM scaffold (Figures 6B and 6C). bIO-Col VI exhibited substantial viability, along with the pronounced expression of key maturation maker genes INS and GCG, and a robust GSIS when compared with bIO (Figures 6D–6F), without significant difference in GCG secretion between bIO and bIO-Col VI (Figure 6G). To investigate the *in vivo* function of the biomimetic islets, we transplanted IO, bIO, and bIO-Col VI into the subcutaneous space in STZ-induced diabetic non-obese diabetic (NOD)-severe combined immuodeficiency (SCID) mice. The engrafted IOs were monitored using luciferase assay for 3 months after the transplantation. As expected, BLI showed significantly higher luciferase expression in the bIO-Col VI group compared with the bIO and IO groups (Figures 6H and 6I). Moreover, the blood glucose levels were effectively restored in bIO-Col VI

(B) Schematic representation of experimental workflow.
(C) Non-fasted blood glucose levels in normal mice and STZ-induced un-transplanted (STZ-no TX), or recipients of aIO, dIO, aIO/dAM sheet, dIO/dAM sheet groups. $n = 6$. $^*p < 0.05$, $^{**}p < 0.01$.
(D) Body weight trajectories of normal mice and STZ-induced un-transplanted, or recipients of aIO, dIO, aIO/dAM sheet, dIO/dAM sheet groups. Data are represented as mean ± SEM. Two-way ANOVA. $n = 6$. $^*p < 0.05$.
(E) The proportion of diabetic mice restored to normoglycemia in recipients of aIO, dIO, aIO/dAM sheet, and dIO/dAM sheet.
(F) Blood glucose levels were measured in diabetic recipients in a glucose tolerance test. Data are represented as mean ± SEM. Two-way ANOVA. $n = 4$. $^{**}p < 0.01$.
(G) ELISA measurements of human C-peptide under fasting and glucose-injected conditions in the serum at 1 and 3 months post-transplantation. Data are represented as mean ± SEM. Two-way ANOVA. $n = 6$. $^*p < 0.05$, $^{**}p < 0.01$, $^{***}p < 0.001$.
(H) Blood glucose levels before and after the surgical removal of the grafts at 3 months in randomly selected recipients of aIO, dIO, dAM/dAM sheet, and dIO/dAM sheet. Data are represented as mean ± SEM. One-way ANOVA. $n = 3$. $^*p < 0.05$.
(I) BLI signals of the grafts at 1 and 3 months post-transplantation.
(J) Comparative analysis of bioluminescence intensity of the grafts at 1 and 3 months post-transplantation. Data are represented as mean ± SEM. Two-way ANOVA $n = 3$. $^*p < 0.05$, $^{***}p < 0.001$.
(K) Representative TUNEL staining images of graft sections at 3 months post-transplantation. Scale bar, 20 μm.
(L) Quantitative assessment of TUNEL-positive nuclei within the grafts. Data are represented as mean ± SEM. Two-way ANOVA. $n = 5$. $^*p < 0.05$, $^{***}p < 0.001$.
(M) Representative immunostaining of HNA and C-peptide in 3 months post-transplantation grafts. Nuclei were counterstained with DAPI. Scale bars, 20 μm.
(N) Representative CD31 and INS immunostaining in the grafts at 3 months post-transplantation. Nuclei were counterstained with DAPI. Scale bars, 20 μm.
See also Figure S5.

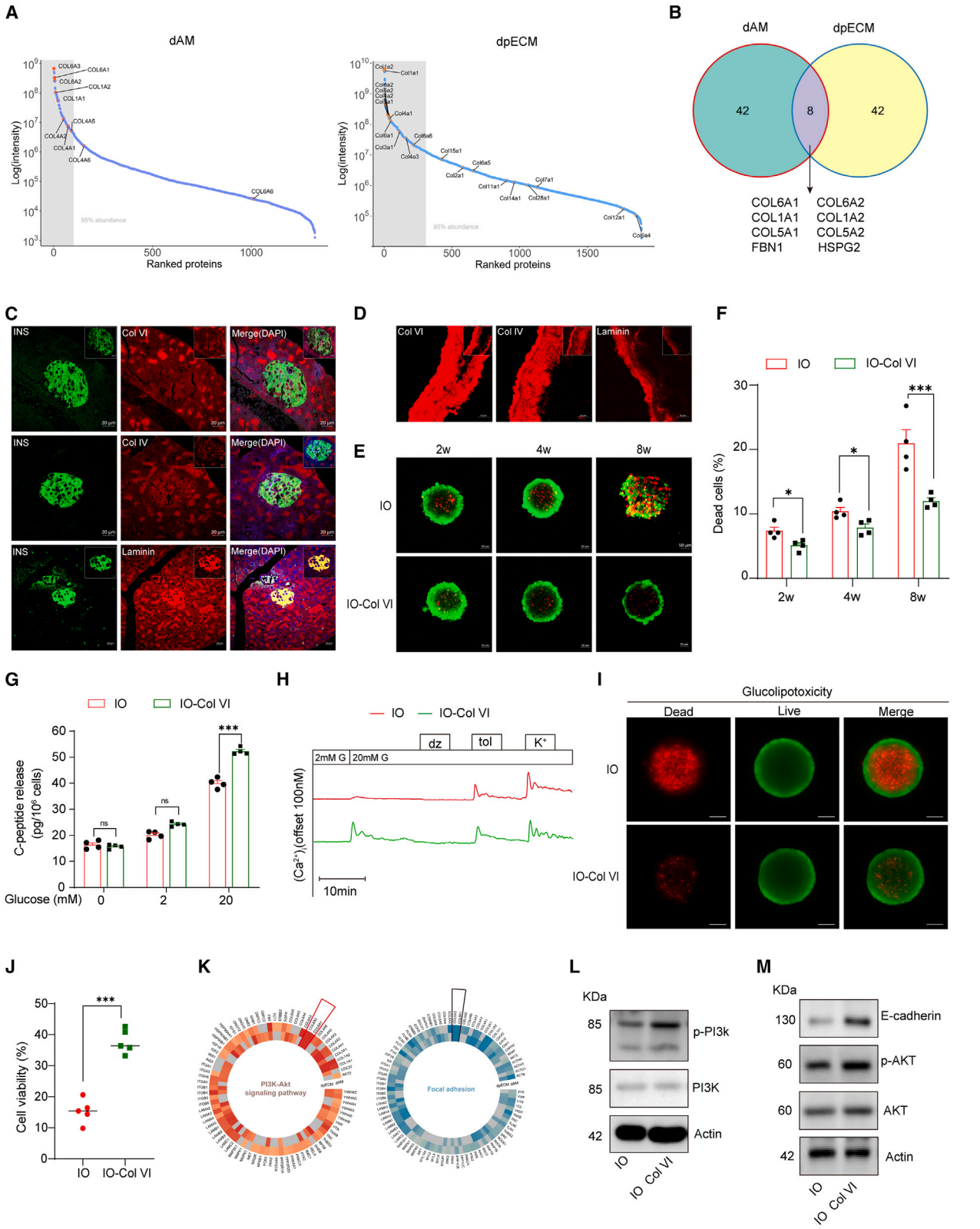

Figure 5. Col VI plays a vital role in sustaining IO viability and function

(A) Proteomic analysis revealed abundant proteins within both dAM and dpECM. The gray-shaded area represents the range covering 95% of the total protein abundance.

(legend continued on next page)

recipients (Figure 6J). IPGTT results showed a quicker recovery to normal blood glucose levels in recipients of bIO-Col VI compared with IO and bIO (Figure 6K). The serum human INS levels were notably the highest in the bIO-Col VI recipients, corroborating the aforementioned findings (Figure 6L). These findings suggested that bIO-Col VI effectively contributes to islet survival, INS secretion, and glycemic control upon subcutaneous transplantation in diabetic mice.

dIO/dAM sheet and bIO-Col VI exhibit cellular composition and endocrine function resembling that of human islets and reverse diabetes in mice

To comprehensively evaluate the optimized hiPSC-derived IOs (dIO/dAM sheet and bIO-Col VI), we conducted morphometric, functional, metabolomic, and engraftment analyses in comparison with human islets. Human islets were isolated from pancreatic tissue and verified by dithizone staining (Figures S7A–S7G). The dIO/dAM sheet and bIO-Col VI demonstrated organotypic cytoarchitecture similar to human islets, as indicated by positive staining for INS, GCG, and SST (Figure 7A). Both dIO/dAM sheet and bIO-Col VI contained approximately 40%–50% INS-positive cells, comparable with the 55%–65% found in human islets. The proportion of GCG-positive cells was reduced in both dIO/dAM sheet (10%–21%) and bIO-Col VI (10%–18%), compared with human islets (20%–30%). SST-positive cells were present at around 5% in both dIO/dAM sheet and bIO-Col VI groups, compared with approximately 10% in human islets (Figure 7B). GSIS assay results revealed that the INS secretion dynamics in both the dIO/dAM sheet and bIO-Col VI were less robust compared with human islets. Nonetheless, both the dIO/dAM sheet and bIO-Col VI demonstrated a gradual increase in INS secretion over time, with a threshold for triggering INS release at approximately 5 mM glucose, similar to that observed in human islets (Figures 7C and 7D). Notably, human islets showed a distinct spike in INS secretion at approximately 5 mM glucose, whereas the dIO/dAM and bIO-Col VI groups exhibited a more gradual increase (Figure 7D).

Considering the metabolic maturation crucial for glucose-stimulated INS release in functional human islets, glucose-induced mitochondrial respiratory assays were performed. Both the dIO/dAM sheet and bIO-Col VI showed increased OCR upon stimulation with high glucose, albeit slightly lower compared with human islets (Figure 7E). Basal OCR in the dIO/dAM sheet and bIO-Col VI was comparable with that of human islets when normalized to DNA content and higher than that of human islets when normalized to C-peptide content (Figure 7F). The capacity of the dIO/dAM sheet and bIO-Col VI to elevate OCR as efficiently as human islets in response to glucose suggests their metabolic maturity and efficient engagement of mitochondrial oxidative phosphorylation.

To determine the functional maturation status of dIO/dAM sheet and bIO-Col VI, we used a fluorescent Ca^{2+} indicator to measure cytoplasmic Ca^{2+} concentration ($[Ca^{2+}]_i$) in individual cells from the dIO/dAM sheet, bIO-Col VI, and human islets. The $[Ca^{2+}]_i$ levels in the dIO/dAM sheet and bIO-Col VI were found to be comparable with human islet cells, displaying a significant and rapid increase in calcium influx when stimulation with high glucose and KCl. Most cells within the dIO/dAM sheet, bIO-Col VI, and human islet demonstrated oscillations in $[Ca^{2+}]_i$ amplitude. Those oscillations were diminished by the opening of K_{ATP} channels with diazoxide and enhanced upon their closure with tolbutamide (Figures 7G and 7H).

To compare the *in vivo* functional dIO/dAM sheet, bIO-Col VI, and human islets, we transplanted them into subcutaneous NOD-SCID mice. We further validated the microvasculature in collected grafts 2 months post-engraftment using TEM. We observed β cells within INS granules accompanied by endothelial cells or vessel structure in the dIO/dAM sheet, bIO-Col VI, and human islets grafts (Figure 7I). Among recipients, mice transplanted with human islets showed the fastest restoration of blood glucose (Figure 7J). Correspondingly, circulating human C-peptide levels were lower in mice grafted with dIO/dAM sheet and bIO-Col VI compared with those with human islets (Figure 7K). Notably, most recipients of the dIO/dAM sheet and bIO-Col VI achieved complete normoglycemia restoration after 2 months, similar to those receiving human islets (Figure 7J). Glucose tolerance tests indicated that glucose clearance was slightly slower in mice engrafted with the dIO/dAM sheet and bIO-Col VI compared with those with human islets. Correspondingly, all types of recipients regulated INS secretion in response to glucose injection (Figures 7L and 7M). The population of endocrine cells in the dIO/dAM sheet, bIO-Col VI, and human islet grafts remained largely unchanged 2 months after transplantation (Figures S7H and S7I). Collectively, we generated dIO/dAM sheet and bIO-Col VI with cellular composition and endocrine function similar to those of human islets, facilitating the rapid reversal of diabetes *in vivo*.

DISCUSSION

IOs derived from PSCs hold great promise in achieving INS-independent therapy for diabetes. In this study, we developed a

(B) Venn diagram depicting the intersection of the top 50 identified proteins common to both dAM and dpECM.
(C) Representative immunostaining of Col IV, Col VI, laminin, and INS in mouse pancreatic tissue sections. Scale bars, 20 μm.
(D) Representative immunostaining of Col IV, Col VI, and laminin in the AM tissue sections. Scale bars, 20 μm.
(E) Live/dead staining of IOs cultured in the presence or absence of Col VI at intervals of 2, 4, and 8 weeks. Scale bars, 50 μm.
(F) Cell death quantification in IO cultured with or without Col VI after 2, 4, and 8 weeks. Data are represented as mean ± SEM. Two-way ANOVA. $n = 4$. $^{*}p < 0.05$, $^{***}p < 0.001$.
(G) Glucose-stimulated C-peptide release assay in IOs cultured with or without Col VI. Data are represented as mean ± SEM. Two-way ANOVA. $n = 4$. $^{***}p < 0.001$.
(H) Representative $[Ca^{2+}]_i$ recordings from IO and IO-Col VI during exposure to 2 and 20 mM glucose, 250 μM diazoxide, 1 mM tolbutamide, and 30 mM K^+.
(I) Live/dead staining of IO and IO-Col VI after exposure to glucolipotoxicity conditions. Scale bars, 50 μm.
(J) Viability quantification post-glucolipotoxicity treatment. Data are represented as mean ± SEM. One-way ANOVA. $n = 5$. $^{***}p < 0.001$.
(K) Identification of Col VI within both dAM and dpECM, highlighting its involvement in PI3K-AKT and focal adhesion signaling pathways.
(L) Representative western blot of indicated proteins.
(M) Representative western blot of indicated proteins.
See also Figure S6 and Table S1.

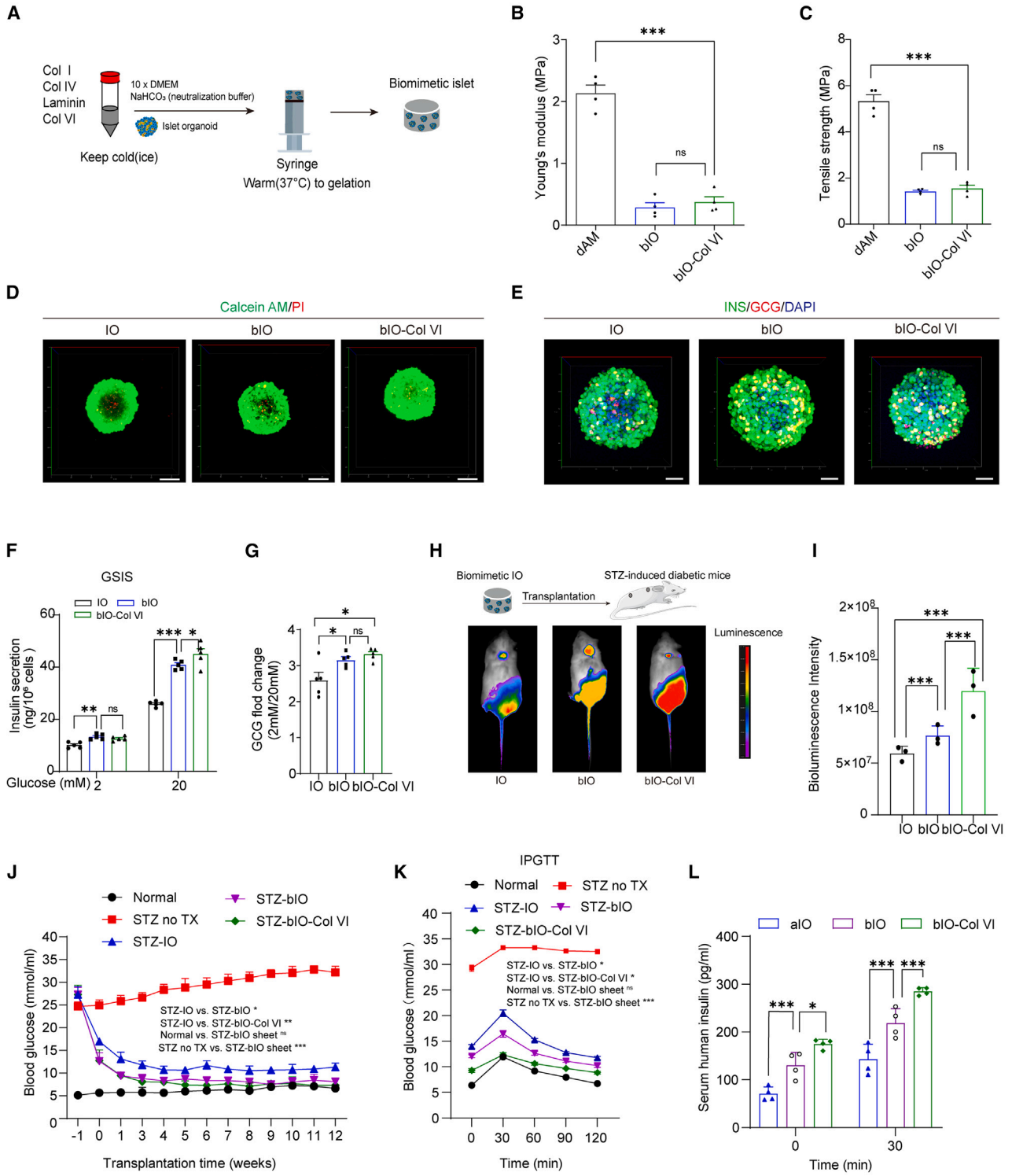

Figure 6. Col VI contribution to biomimetic islet structure and physiological function

(A) Schematic representation of ECM scaffold engineering for IOs construction.

(B) Mechanical property assessment of decellularized AM (dAM), biomimetic IOs (bIO), and bIO with Col VI integration (bIO-Col VI) determined by Young's modulus.

(C) Tensile strength evaluation for dAM, bIO, and bIO-Col VI to measure mechanical integrity.

(D) Live/dead staining for IOs of IO, bIO, and bIO-Col VI. Scale bars, 100 μm.

(E) Immunostaining of INS and GCG in IO, bIO, and bIO-Col VI. Scale bars, 50 μm.

(legend continued on next page)

feasible approach to generate productive and homogeneous IOs with high viability and functionality from hiPSCs. IOs cultured on the dAM sheet exhibited improved engraftment, which was highly vascularized and rapidly restored normal glycemia. We further identified Col VI as a key component that supports IO viability and INS secretion. Moreover, biomimetic ECM containing Col VI exhibited architectural and physiological features favorable for the survival and maturation of IOs, which in turn successfully reversed the hyperglycemia in diabetic mice.

The microwell platform provides several advantages, including homogeneity in cluster size and morphology, better cell stability, and scaling-up suitability. Our approach is similar to a recent report, which confirms the versatility of the microwell system in facilitating the formation of pancreatic duct-like organoids.[17] The dAM ECM contains various biomolecules, such as brain-derived neurotrophic factor (BDNF) and EGF, which prevent cell apoptosis.[12] Despite the survival and function of hiPSC-derived IOs relying primarily on WNT, EGF, Notch, and TGF-β signaling, there is no doubt that the extracellular components of dAM also contribute considerably to the survival and maturity of IOs, based on the findings in this study. Likewise, our findings are supported by previous studies, which highlight the significant impact of organ-specific ECM on stem cell fate.[7,18,19]

Islet transplantation, a clinical procedure typically involving the delivery of islets into the liver via the portal vein, often exposes the transplanted islets to detrimental environments, such as hypoxia and inflammation, inevitably resulting in significant loss of the transplants.[20] Islet transplantation into kidney capsules has been shown to be an efficient treatment for diabetes. However, it is deemed not suitable for human patients. Alternatively, transplantation has been performed subcutaneously, intramuscularly, intraperitoneally, and within the omentum.[21,22] A recent study showed that transplantation of stem-cell-derived IOs into the anterior rectus sheath also effectively restores normoglycemia in experimental diabetes in monkeys.[23] For phase 1 clinical trials, the subcutaneous region was chosen despite its lack of an extensive vascular network. Advantages such as operational simplicity, reduced trauma, and ease of monitoring and retrieval make it an excellent option. Evidence accumulated from numerous studies suggests that the survival of the engrafted organoids could be further enhanced through the integration of endothelial cells, mesenchymal stem cells, microvessels, or materials. These advancements offer promising translational applications to meet the clinical needs.[24–26]

The prevailing challenge hindering the efficacy of islet transplantation is the diminished long-term survival after engraftment. This predicament is primarily attributed to either substandard vascularization or an onslaught from host immune cells.[24] Efforts aiming to preserve islet cell viability and functionality were made extensively.[16,27] AM has been frequently illustrated in promoting angiogenesis in skin wound healing.[28,29] Two potential mechanisms underlie the success of dIO/dAM sheet in alleviating hyperglycemia. First, the dAM hosts an array of intrinsic bioactive factors that positively regulate islet cell survival and INS secretion. In addition, the behavior of endothelial cells and the formation of blood vessels on IOs are modulated by the matrix proteins of dAM. These organoids proficiently rectify hyperglycemia in diabetic mice, producing outcomes akin to those observed with 3D-printed hyaluronic acid methacrylate (HAMA)/pECM IOs, which maintained prolonged blood glucose stability.[15,30]

The interaction between β cells and the ECM has been meticulously inspected. Deficiencies of ECM components have been implicated in impaired islet viability and function.[14] Evidence from the literature suggests that Col IV engages with the α1β1 integrin on pancreatic β cells, thereby facilitating INS secretion and enhancing β cell differentiation and survival.[31,32] Recent revelations propose Col VI as a critical structural component within the cell niche.[33] Unambiguously, Col VI has been identified as the central element of the human islet ECM/niche, present in quantities exceeding twice that of Col I and IV.[34] Evidence on the influence of Col VI on islet development, survival, and function remains scarce. It is worth noting that Col VI is the predominant subtype of ECM encapsulating islet in the pancreas, offering potential benefits over other ECM types.[35] Our study reiterates the indispensable role of Col VI in upholding not only the structural integrity but also the functionality and longevity of IO engraftment. Our data substantiate the previous study suggesting an enhancement of β cell activity by Col VI.[36,37]

The effectiveness of specific ECM properties along with mechanical attributes is paramount in shaping the microenvironment, directing the differentiation of iPSC or embryonic stem cells (ESCs) into IOs, while simultaneously buttressing islet survival and functionality. Our study further corroborates the supportive role of Col VI in biomimetic islets. These biomimetically fashioned IOs optimally mirror facets of the native microenvironment and maximize the inherent islet traits. We illustrated that the generation of such biomimetic islets could improve transplantation outcomes, offering a potentially therapeutic solution for diabetes. Notably, our study confirms that optimized hiPSC-derived IOs (including dIO/dAM sheet and bIO-Col VI) exhibit cellular composition and endocrine function comparable with those of human islets. The endocrine functions of these organoids closely mimic those of native human islets, consistent with previous findings.[4,5] Furthermore, these hiPSC-derived IOs effectively reverse diabetes *in vivo*.

(F) GSIS of IO, bIO, and bIO-Col VI. Data are represented as mean ± SEM. Two-way ANOVA. $n = 5$. $^{*}p < 0.05$, $^{**}p < 0.01$, $^{***}p < 0.001$.
(G) GCG secretion response to glucose stimulation in IO, bIO, and bIO-Col VI. Data are represented as mean ± SEM. Two-way ANOVA. $n = 5$. $^{*}p < 0.05$.
(H) Bioluminescence monitoring of transplanted IO, bIO, and bIO-Col VI in diabetic mice.
(I) Comparative analysis of bioluminescence intensity of IO, bIO, bIO-Col VI grafts at 3 months post-transplantation. Data are represented as mean ± SEM. Two-way ANOVA. $n = 3$. $^{***}p < 0.001$.
(J) Blood glucose levels post-transplantation in diabetic mice among IO, bIO, and bIO-Col VI groups. Data are represented as mean ± SEM. Two-way ANOVA. $n = 5$. $^{*}p < 0.05$, $^{**}p < 0.01$, $^{***}p < 0.001$.
(K) Blood glucose concentrations were assessed during an IPGTT at 4 weeks post-transplantation. Data are represented as mean ± SEM. Two-way ANOVA. $n = 3$. $^{*}p < 0.05$, $^{**}p < 0.01$, $^{***}p < 0.001$.
(L) Human C-peptide concentrations were measured during an IPGTT at 4 weeks following transplantation. Data are represented as mean ± SEM. Two-way ANOVA. $n = 4$. $^{*}p < 0.05$, $^{***}p < 0.001$.

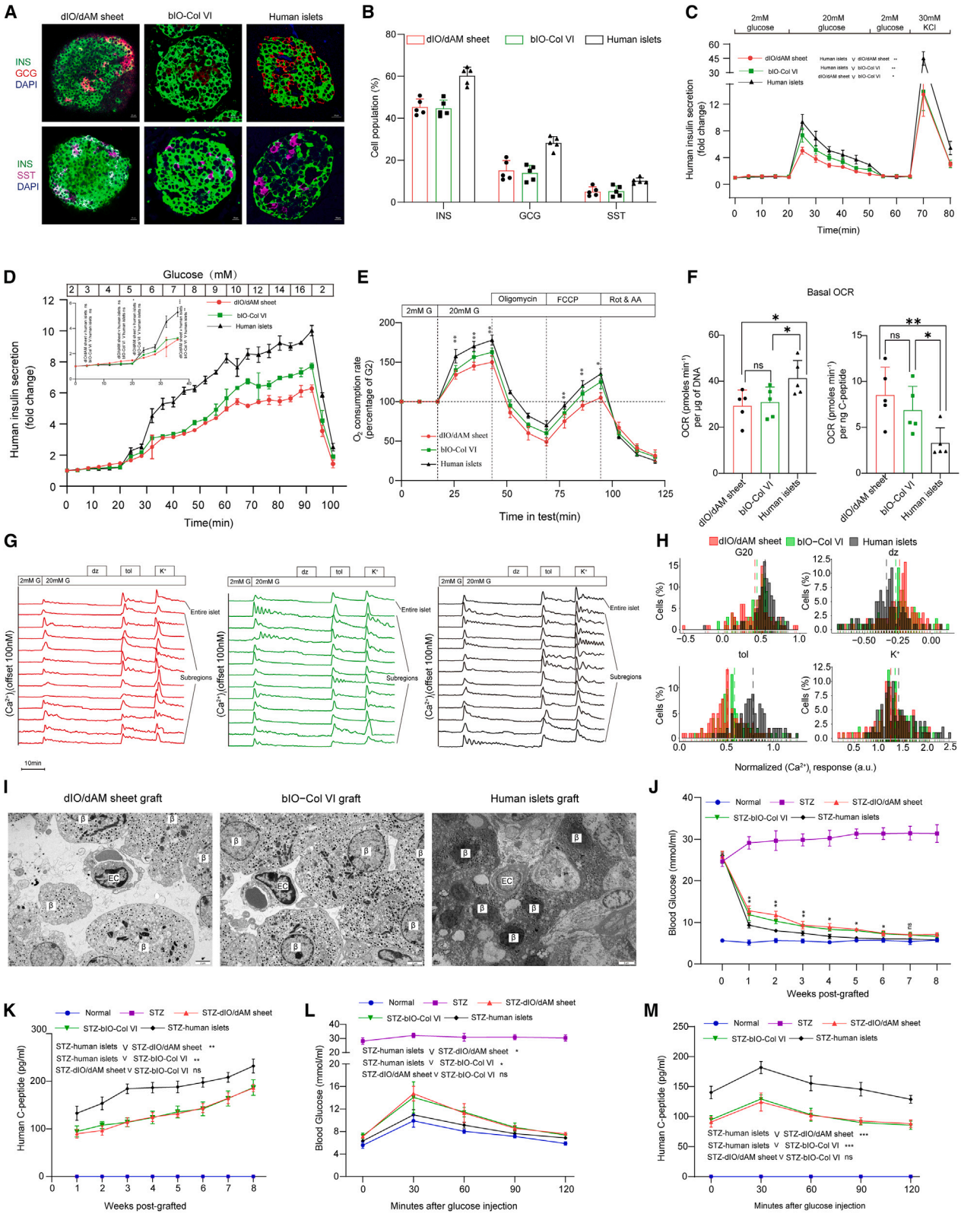

(legend on next page)

In conclusion, our study highlights the significant role played by dAM ECM hydrogel in supporting islet development, survival, and functional maturity. The dAM sheet, capable of anchoring IOs, aids in preserving islet homeostasis, extending glucose response, and rapidly reversing hyperglycemia in diabetic mice. In particular, we identified Col VI as a positive influencer of long-term survival and functional preservation for iPSC-derived IOs. An effective biomimetic ECM engineered to foster islets exhibited beneficial architecture and functionality. Furthermore, the cellular composition and endocrine function of optimized iPSC-derived IOs are comparable with those of human islets. Consequently, our study provides a valuable platform for generating productive IOs with elevated viability and robust functionality, potentially instrumental in drug discovery and cell transplantation therapy for diabetes.

Limitations of the study

The experimental systems employed in this study present certain limitations worthy of consideration. Variability is observed within batches of IOs derived from hiPSCs. Such variability is a predictable outcome, given the sophisticated 27-day, 5-stage protocol incorporating differentiation media amalgamated with growth factors to which the cells were subjected. The multistage nature of our differentiation protocol, encompassing 5 stages, can indeed introduce potential failure points that might impede the successful generation of IOs. Indeed, this variability was also evident within the batches of dAM. Furthermore, the methodology employed did not precisely assess β cell functionality: rather than isolating and analyzing pure β cells, measurements were taken from whole IOs. Thus, these parameters should be considered when interpreting results yielded by such experimental systems. A comprehensive understanding of the potential role of dAM in hiPSC differentiation into IOs would necessitate more advanced methodologies, such as high-throughput proteomics analysis or single-cell RNA sequencing.

RESOURCE AVAILABILITY

Lead contact

Further information and requests for resources and reagents should be directed to and will be fulfilled by the lead contact, Guoxiang Jin (gxjinking@163.com).

Materials availability

This study did not generate new unique reagents.

Data and code availability

The proteomics data generated during this study are available at ProteomeXchange Consortium (PRIDE: PXD047565). No original code is reported in this paper.

ACKNOWLEDGMENTS

This work was funded by grants from National Natural Science Foundation of China (81821003, 82273180, 82472713, and 81972774), Natural Science Foundation of Guangdong Province (2024A1515011365), Science and Technology Projects in Guangzhou (2025A03J4509), Guangdong Provincial People's Hospital, High-level Hospital Construction Project (KJ012021074 and KJ012019517), and Guangdong Basic and Applied Basic Research Foundation (2021B1515130004). We express our gratitude to all laboratory members for their invaluable insights and recommendations regarding this study. Our thanks extend to Pengju Lou for his diligent care of the animals. We extend our sincere thanks to Professors Jiansu Chen, Jun Zhang, and Ling Zhao for their technical assistance. We appreciate Jingwen Dai's assistance with supplying human amniotic membrane samples. The graphical abstract was primarily created using BioRender.com.

AUTHOR CONTRIBUTIONS

G.J. and Z.Z. conceived and designed the project. D.Z. performed most of the experiments, collected and analyzed the data, wrote the manuscript, and took full responsibility for the article and its originality. Z.C. was involved in data

Figure 7. dIO/dAM sheet and bIO-Col VI exhibit cellular composition and endocrine function resembling that of human islets and reverse diabetes in mice

(A) Immunostaining images of dIO/dAM sheet, bIO-Col VI, and human islets depicting markers for INS (β cells), GCG (α cells), and SST (δ cells).

(B) Quantitative analysis of INS, GCG, and SST positive cells in dIO/dAM sheet, bIO-Col VI, and human islets. Data presented as mean ± SEM. Two-way ANOVA. $n = 5$.

(C) GSIS assay results from dIO/dAM sheet, bIO-Col VI, and human islets perfused with 2–20 mM glucose and 30 mM KCl, normalized to secretion during the first 16 min. Two-way ANOVA. $n = 4$–6. $^{*}p < 0.05$, $^{**}p < 0.01$.

(D) INS secretion response to a gradual increase in glucose concentration from 2 to 16 mM, normalized to secretion during the first 8 min. Two-way ANOVA. $^{*}p < 0.05$, $^{**}p < 0.01$.

(E) OCR changes in response to 20 mM glucose, 5 μM oligomycin, 1 μM carbonyl cyanide-4 (trifluoromethoxy) phenylhydrazone (FCCP), and 5 μM rotenone + antimycin A. Data presented as mean ± SEM. Two-way ANOVA. $^{*}p < 0.05$, $^{**}p < 0.01$.

(F) Basal OCR of dIO/dAM sheet, bIO-Col VI, and human islets. Data presented as mean ± SEM. Two-way ANOVA. $^{*}p < 0.05$, $^{**}p < 0.01$.

(G) Representative $[Ca^{2+}]_i$ recordings from dIO/dAM sheet, bIO-Col VI, and human islets during exposure to 2 and 20 mM glucose, 250 μM diazoxide, 1 mM tolbutamide, and 30 mM K^+.

(H) Histograms illustrating changes in $[Ca^{2+}]_i$ normalized to levels at 2 mM glucose in cells from dIO/dAM sheet, bIO-Col VI, and human islets.

(I) Electron micrographs of dIO/dAM sheet, bIO-Col VI, and human islets grafts 8 weeks post-transplantation.

(J) Non-fasted blood glucose levels in control mice without STZ induction, un-transplanted mice (normal) and STZ-induced un-transplanted (STZ), or those transplanted with dIO/dAM sheet (STZ-dIO/dAM sheet), bIO-Col VI (STZ-bIO-Col VI), or human islets (STZ-human islets). Data are represented as mean ± SEM. Two-way ANOVA. $n = 6$. $^{*}p < 0.05$, $^{**}p < 0.01$.

(K) Human-specific C-peptide levels in recipients of dIO/dAM sheet, bIO-Col VI, and human islets. Data are represented as mean ± SEM. Two-way ANOVA. $n = 4$. $^{**}p < 0.01$.

(L) Blood glucose levels were measured during a glucose tolerance test in recipients of dIO/dAM sheet, bIO-Col VI, and human islets. Data are represented as mean ± SEM. Two-way ANOVA. $n = 4$. $^{*}p < 0.05$.

(M) ELISA measurements of human C-peptide in the serum of diabetic mice at 2 months post-transplantation with dIO/dAM sheet, bIO-Col VI, and human islets under glucose-injected conditions. Data are represented as mean ± SEM. Two-way ANOVA. $n = 6$. $^{***}p < 0.001$.

See also Figure S7.

analyses. K.G., Q.X., Y.Z., and Q.M. provided support for the experimental work. G.J. and Z.Z. reviewed and edited the manuscript and supervised the project. All authors read and approved the final version of the manuscript.

DECLARATION OF INTERESTS

The authors declare no competing interests.

STAR★METHODS

Detailed methods are provided in the online version of this paper and include the following:

- KEY RESOURCES TABLE
- EXPERIMENTAL MODEL AND STUDY PARTICIPANT DETAILS
  - Animals
  - Decellularized amniotic membrane
  - Human islets
- METHOD DETAILS
  - Cell culture and cell differentiation
  - Karyotype analysis
  - Viability assessment
  - ATP measurement
  - Western blotting
  - Histology and immunostaining
  - Ex vivo static and dynamic glucose-stimulated insulin secretion (GSIS)
  - Enzyme-linked immunosorbent assay (ELISA)
  - Calcium imaging
  - Flow cytometry
  - Mitochondrial respiration measurement
  - Transmission electron microscopy
  - Scanning electron microscopy
  - TUNEL staining
  - Cryopreservation and recovery of hiPSC-islet organoids
  - Glucolipotoxicity
  - Subcutaneous transplantation
  - Intraperitoneal glucose tolerance test (IPGTT)
  - Bioluminescence monitoring of transplanted islet organoids
  - High performance liquid chromatography-tandem mass spectrometry (HPLC-MS/MS)
  - Engineering biomimetic ECM scaffold for islet organoids
  - Mechanical properties
  - Dithizone staining
- QUANTIFICATION AND STATISTICAL ANALYSIS

SUPPLEMENTAL INFORMATION

Supplemental information can be found online at https://doi.org/10.1016/j.stem.2025.02.001.

Received: January 10, 2024
Revised: September 10, 2024
Accepted: February 3, 2025
Published: February 24, 2025

REFERENCES

1. Sun, H., Saeedi, P., Karuranga, S., Pinkepank, M., Ogurtsova, K., Duncan, B.B., Stein, C., Basit, A., Chan, J.C., Mbanya, J.C., et al. (2022). IDF Diabetes Atlas: Global, regional and country-level diabetes prevalence estimates for 2021 and projections for 2045. Diabetes Res. Clin. Pract. *183*, 109119. https://doi.org/10.1016/j.diabres.2021.109119.
2. Saeedi, P., Petersohn, I., Salpea, P., Malanda, B., Karuranga, S., Unwin, N., Colagiuri, S., Guariguata, L., Motala, A.A., Ogurtsova, K., et al. (2019). Global and regional diabetes prevalence estimates for 2019 and projections for 2030 and 2045: Results from the International Diabetes Federation Diabetes Atlas, 9th edition. Diabetes Res. Clin. Pract. *157*, 107843. https://doi.org/10.1016/j.diabres.2019.107843.
3. Shapiro, A.M.J., Ricordi, C., Hering, B.J., Auchincloss, H., Lindblad, R., Robertson, R.P., Secchi, A., Brendel, M.D., Berney, T., Brennan, D.C., et al. (2006). International trial of the Edmonton protocol for islet transplantation. N. Engl. J. Med. *355*, 1318–1330. https://doi.org/10.1056/NEJMoa061267.
4. Balboa, D., Barsby, T., Lithovius, V., Saarimäki-Vire, J., Omar-Hmeadi, M., Dyachok, O., Montaser, H., Lund, P.-E., Yang, M., Ibrahim, H., et al. (2022). Functional, metabolic and transcriptional maturation of human pancreatic islets derived from stem cells. Nat. Biotechnol. *40*, 1042–1055. https://doi.org/10.1038/s41587-022-01219-z.
5. Nair, G.G., Liu, J.S., Russ, H.A., Tran, S., Saxton, M.S., Chen, R., Juang, C., Li, M.-L., Nguyen, V.Q., Giacometti, S., et al. (2019). Recapitulating endocrine cell clustering in culture promotes maturation of human stem-cell-derived β cells. Nat. Cell Biol. *21*, 263–274. https://doi.org/10.1038/s41556-018-0271-4.
6. Pagliuca, F.W., Millman, J.R., Gürtler, M., Segel, M., Van Dervort, A., Ryu, J.H., Peterson, Q.P., Greiner, D., and Melton, D.A. (2014). Generation of functional human pancreatic β cells in vitro. Cell *159*, 428–439. https://doi.org/10.1016/j.cell.2014.09.040.
7. Bi, H., Ye, K., and Jin, S. (2020). Proteomic analysis of decellularized pancreatic matrix identifies collagen V as a critical regulator for islet organogenesis from human pluripotent stem cells. Biomaterials *233*, 119673. https://doi.org/10.1016/j.biomaterials.2019.119673.
8. Citro, A., Moser, P.T., Dugnani, E., Rajab, T.K., Ren, X., Evangelista-Leite, D., Charest, J.M., Peloso, A., Podesser, B.K., Manenti, F., et al. (2019). Biofabrication of a vascularized islet organ for type 1 diabetes. Biomaterials *199*, 40–51. https://doi.org/10.1016/j.biomaterials.2019.01.035.
9. Willenberg, B.J., Oca-Cossio, J., Cai, Y., Brown, A.R., Clapp, W.L., Abrahamson, D.R., Terada, N., Ellison, G.W., Mathews, C.E., Batich, C.D., et al. (2015). Repurposed biological scaffolds: kidney to pancreas. Organogenesis *11*, 47–57. https://doi.org/10.1080/15476278.2015.1067354.
10. Giobbe, G.G., Crowley, C., Luni, C., Campinoti, S., Khedr, M., Kretzschmar, K., De Santis, M.M., Zambaiti, E., Michielin, F., Meran, L., et al. (2019). Extracellular matrix hydrogel derived from decellularized tissues enables endodermal organoid culture. Nat. Commun. *10*, 5658. https://doi.org/10.1038/s41467-019-13605-4.
11. Hu, Z., Luo, Y., Ni, R., Hu, Y., Yang, F., Du, T., and Zhu, Y. (2023). Biological importance of human amniotic membrane in tissue engineering and regenerative medicine. Mater. Today Bio *22*, 100790. https://doi.org/10.1016/j.mtbio.2023.100790.
12. Yang, Z., Li, X., Zhang, C., Sun, N., Guo, T., Lin, J., Li, F., and Zhang, J. (2020). Amniotic membrane extract protects islets from serum-deprivation induced impairments and improves islet transplantation outcome. Front. Endocrinol. *11*, 587450. https://doi.org/10.3389/fendo.2020.587450.
13. Lebreton, F., Lavallard, V., Bellofatto, K., Bonnet, R., Wassmer, C.H., Perez, L., Kalandadze, V., Follenzi, A., Boulvain, M., Kerr-Conte, J., et al. (2019). Insulin-producing organoids engineered from islet and amniotic epithelial cells to treat diabetes. Nat. Commun. *10*, 4491. https://doi.org/10.1038/s41467-019-12472-3.
14. Santini-González, J., Simonovich, J.A., Castro-Gutiérrez, R., González-Vargas, Y., Abuid, N.J., Stabler, C.L., Russ, H.A., and Phelps, E.A. (2021). In vitro generation of peri-islet basement membrane-like structures. Biomaterials *273*, 120808. https://doi.org/10.1016/j.biomaterials.2021.120808.
15. Wang, D., Guo, Y., Zhu, J., Liu, F., Xue, Y., Huang, Y., Zhu, B., Wu, D., Pan, H., Gong, T., et al. (2023). Hyaluronic acid methacrylate/pancreatic extracellular matrix as a potential 3D printing bioink for constructing islet organoids. Acta Biomater. *165*, 86–101. https://doi.org/10.1016/j.actbio.2022.06.036.
16. Patel, S.N., Ishahak, M., Chaimov, D., Velraj, A., LaShoto, D., Hagan, D.W., Buchwald, P., Phelps, E.A., Agarwal, A., and Stabler, C.L. (2021).

Organoid microphysiological system preserves pancreatic islet function within 3D matrix. Sci. Adv. *7*, eaba5515. https://doi.org/10.1126/sciadv.aba5515.

17. Wiedenmann, S., Breunig, M., Merkle, J., von Toerne, C., Georgiev, T., Moussus, M., Schulte, L., Seufferlein, T., Sterr, M., Lickert, H., et al. (2021). Single-cell-resolved differentiation of human induced pluripotent stem cells into pancreatic duct-like organoids on a microwell chip. Nat. Biomed. Eng. *5*, 897–913. https://doi.org/10.1038/s41551-021-00757-2.
18. Berger, C., Bjørlykke, Y., Hahn, L., Mühlemann, M., Kress, S., Walles, H., Luxenhofer, R., Ræder, H., Metzger, M., and Zdzieblo, D. (2020). Matrix decoded – A pancreatic extracellular matrix with organ specific cues guiding human iPSC differentiation. Biomaterials *244*, 119766. https://doi.org/10.1016/j.biomaterials.2020.119766.
19. Cozzitorto, C., Mueller, L., Ruzittu, S., Mah, N., Willnow, D., Darrigrand, J.-F., Wilson, H., Khosravinia, D., Mahmoud, A.-A., Risolino, M., et al. (2020). A specialized niche in the pancreatic microenvironment promotes endocrine differentiation. Dev. Cell *55*, 150–162.e6. https://doi.org/10.1016/j.devcel.2020.08.003.
20. Pepper, A.R., Bruni, A., and Shapiro, A.M.J. (2018). Clinical islet transplantation: is the future finally now? Curr. Opin. Organ Transplant. *23*, 428–439. https://doi.org/10.1097/MOT.0000000000000546.
21. Bertuzzi, F., Colussi, G., Lauterio, A., and De Carlis, L. (2018). Intramuscular islet allotransplantation in type 1 diabetes mellitus. Eur. Rev. Med. Pharmacol. Sci. *22*, 1731–1736. https://doi.org/10.26355/eurrev_201803_14588.
22. Migliorini, A., Nostro, M.C., and Sneddon, J.B. (2021). Human pluripotent stem cell-derived insulin-producing cells: A regenerative medicine perspective. Cell Metab. *33*, 721–731. https://doi.org/10.1016/j.cmet.2021.03.021.
23. Liang, Z., Sun, D., Lu, S., Lei, Z., Wang, S., Luo, Z., Zhan, J., Wu, S., Jiang, Y., Lu, Z., et al. (2023). Implantation underneath the abdominal anterior rectus sheath enables effective and functional engraftment of stem-cell-derived islets. Nat. Metab. *5*, 29–40. https://doi.org/10.1038/s42255-022-00713-7.
24. Aghazadeh, Y., Poon, F., Sarangi, F., Wong, F.T., Khan, S.T., Sun, X., Hatkar, R., Cox, B.J., Nunes, S.S., and Nostro, M.C. (2021). Microvessels support engraftment and functionality of human islets and hESC-derived pancreatic progenitors in diabetes models. Cell Stem Cell *28*, 1936–1949.e8. https://doi.org/10.1016/j.stem.2021.08.001.
25. Nalbach, L., Roma, L.P., Schmitt, B.M., Becker, V., Körbel, C., Wrublewsky, S., Pack, M., Später, T., Metzger, W., Menger, M.M., et al. (2021). Improvement of islet transplantation by the fusion of islet cells with functional blood vessels. EMBO Mol. Med. *13*, e12616. https://doi.org/10.15252/emmm.202012616.
26. Yoshihara, E., O'Connor, C., Gasser, E., Wei, Z., Oh, T.G., Tseng, T.W., Wang, D., Cayabyab, F., Dai, Y., Yu, R.T., et al. (2020). Immune-evasive human islet-like organoids ameliorate diabetes. Nature *586*, 606–611. https://doi.org/10.1038/s41586-020-2631-z.
27. Zhan, L., Rao, J.S., Sethia, N., Slama, M.Q., Han, Z., Tobolt, D., Etheridge, M., Peterson, Q.P., Dutcher, C.S., Bischof, J.C., et al. (2022). Pancreatic islet cryopreservation by vitrification achieves high viability, function, recovery and clinical scalability for transplantation. Nat. Med. *28*, 798–808. https://doi.org/10.1038/s41591-022-01718-1.
28. Farzan, R., Moeinian, M., Abdollahi, A., Jahangard-Rafsanjani, Z., Alipour, A., Ebrahimi, M., and Khorasani, G. (2018). Effects of amniotic membrane extract and deferoxamine on angiogenesis in wound healing: an in vivo model. J. Wound Care *27* (*Suppl 6*), S26–S32. https://doi.org/10.12968/jowc.2018.27.Sup6.S26.
29. Arrizabalaga, J.H., and Nollert, M.U. (2018). Human amniotic membrane: a versatile scaffold for tissue engineering. ACS Biomater. Sci. Eng. *4*, 2226–2236. https://doi.org/10.1021/acsbiomaterials.8b00015.
30. Duin, S., Schütz, K., Ahlfeld, T., Lehmann, S., Lode, A., Ludwig, B., and Gelinsky, M. (2019). 3D Bioprinting of Functional Islets of Langerhans in an Alginate/Methylcellulose Hydrogel Blend. Adv. Healthc. Mater. *8*, e1801631. https://doi.org/10.1002/adhm.201801631.
31. Riopel, M., Krishnamurthy, M., Li, J., Liu, S., Leask, A., and Wang, R. (2011). Conditional β1-integrin-deficient mice display impaired pancreatic β cell function. J. Pathol. *224*, 45–55. https://doi.org/10.1002/path.2849.
32. Kaido, T., Yebra, M., Cirulli, V., and Montgomery, A.M. (2004). Regulation of human β-cell adhesion, motility, and insulin secretion by collagen IV and its receptor α1β1. J. Biol. Chem. *279*, 53762–53769. https://doi.org/10.1074/jbc.M411202200.
33. Groulx, J.-F., Gagné, D., Benoit, Y.D., Martel, D., Basora, N., and Beaulieu, J.-F. (2011). Collagen VI is a basement membrane component that regulates epithelial cell–fibronectin interactions. Matrix Biol. *30*, 195–206. https://doi.org/10.1016/j.matbio.2011.03.002.
34. Hughes, S.J., Clark, A., McShane, P., Contractor, H.H., Gray, D.W., and Johnson, P.R. (2006). Characterisation of collagen VI within the islet-exocrine interface of the human pancreas: implications for clinical islet isolation? Transplantation *81*, 423–426. https://doi.org/10.1097/01.tp.0000197482.91227.df.
35. Hughes, S.J., McShane, P., Contractor, H.H., Gray, D.W., Clark, A., and Johnson, P.R. (2005). Comparison of the collagen VI content within the islet-exocrine interface of the head, body, and tail regions of the human pancreas. Transplant. Proc. *37*, 3444–3445. https://doi.org/10.1016/j.transproceed.2005.09.027.
36. Llacua, L.A., Hoek, A., de Haan, B.J., and de Vos, P. (2018). Collagen type VI interaction improves human islet survival in immunoisolating microcapsules for treatment of diabetes. Islets *10*, 60–68. https://doi.org/10.1080/19382014.2017.1420449.
37. Wang, H., Li, S., Dai, Q., Gonzalez, A., Tran, O.N., Sun, H., DeFronzo, R.A., Dean, D.D., Yeh, C.-K., and Chen, X.-D. (2020). Culture on a native bone marrow-derived extracellular matrix restores the pancreatic islet basement membrane, preserves islet function, and attenuates islet immunogenicity. FASEB J. *34*, 8044–8056. https://doi.org/10.1096/fj.201902893R.

STAR★METHODS

KEY RESOURCES TABLE

REAGENT or RESOURCE	SOURCE	IDENTIFIER
Antibodies		
Rabbit anti-Sox2	Abcam	Cat #: ab92494; RRID: AB_10585428
Mouse anti-Nanog	Abcam	Cat #: ab62734; RRID: AB_956161
Rabbit anti-Oct4	Abcam	Cat #: ab181557; RRID: AB_2687916
Mouse anti-SEEA4	Abcam	Cat #: ab16287; RRID: AB_778073
Mouse anti-Actin	Reijing Ray Antibody Biotech	Cat #: Rm2001; RRID: AB_2756462
Rabbit anti-Bax	Immunoway	Cat #: YT0455; RRID: AB_3073634
Mouse anti-BCL2	Immunoway	Cat #: YM3041; RRID: AB_2814758
Rabbit anti-Glucagon	Cell Signaling Technology	Cat #: 2760; RRID: AB_659831
Rabbit anti-C-Peptide	Cell Signaling Technology	Cat #: 4593; RRID: AB_10691857
Rat anti-Somatostatin	Millipore Sigma	Cat #: MAB354; RRID: AB_3073635
Insulin	Santa Cruz Biotechnology	Cat #: SC-8033; RRID: AB_627285
NKX6.1	Cell Signaling Technology	Cat #: 54551; RRID: AB_2722625
FoxA2	Cell Signaling Technology	Cat #: 8186; RRID: AB_10891055
SOX17	Cell Signaling Technology	Cat #: 81778; RRID: AB_2650582
PDX1	Abcam	Cat #: ab219207; RRID: AB_ 2891187
Neurogenin3	Santa Cruz Biotechnology	Cat #: SC-376607; RRID: AB_ 11150138
MAFA	Santa Cruz Biotechnology	Cat #: SC-390491; RRID: AB_30736639
E-cadherin	Santa Cruz Biotechnology	Cat #: YT1454; RRID: AB_3073633
Tubulin	Proteintech	Cat #: 11224-1-ap; RRID: AB_2210206
HNA	Abcam	Cat #: ab191181; RRID: AB_2885016
CD31	Abcam	Cat #: ab24590; RRID: AB_448167
PI3K	Affinity	Cat #: Af6241; RRID: AB_2835340
p-PI3K	Affinity	Cat #: Af3241; RRID: AB_2834667
AKT	Cell Signaling Technology	Cat #: 9272; RRID: AB_329827
P-AKT	Cell Signaling Technology	Cat #: 4060; RRID: AB_2315049
GLUT1	Immunoway	Cat #: YT1928; RRID: AB_3073641
SLC18A1	PA5-85975	Cat #: PA5-85975; RRID: AB_2802776
DDC	R&D SYSTEMS	Cat #: AF3564; RRID: AB_2846878
TPH1	Cusabio Technology Llc	Cat #: YT1928; RRID: AB_3073641
FEV	Thermo Fisher Scientific	Cat #: PA5-98805; RRID: AB_2813418
CD45	Biolegend	Cat #: 157214; RRID: AB_2894427
CD3	Biolegend	Cat #: 100218; RRID: AB_1595597
CD19	Biolegend	Cat #: 152412; RRID: AB_2922473
NK1.1	Biolegend	Cat #: 108714; RRID: AB_389363
Collagen I	Abcam	Cat #: ab138492; RRID: AB_2861258
Collagen IV	Proteintech	Cat #: 19674-1-ap; RRID: AB_2878595
Collagen VI	Abcam	Cat #: ab182744; RRID: AB_2847919
Laminin	Sigma-Aldrich	Cat #: L9393-100UL; RRID: AB_3073642
Anit-mouse Alex fluor 488	Thermo Fisher Scientific	Cat # A-11029; RRID: AB_2534088
Anti-rabbit Alex fluor 594	Thermo Fisher Scientific	Cat # A-11037; RRID: AB_2534095
Anti-rat Alex fluor 647	Thermo Fisher Scientific	Cat # A21247; RRID: AB_141778
Biological samples		
Placenta/Amniotic membrane	Guangzhou Women and Children's Medical Center	N/A

(*Continued on next page*)

Continued

REAGENT or RESOURCE	SOURCE	IDENTIFIER
Human islets	Guangdong Provincial People's Hospital or First Affiliated Hospital of Guangzhou Medical University	N/A
Chemicals, peptides, and recombinant proteins		
BME2	R&D System	Cat #: 3533-005-02
N21-max	R&D System	Cat #: AR008
N2-max	R&D System	Cat #: 1612798
Activin A	R&D System	Cat #: 338-AC-010
CHIR 99021	Tocris	Cat #: 252917-06-9
Exendin-4	Tocris	Cat #: 141758-74-9
Nicotinamide	Tocris	Cat #: 98-92-0
KGF-FGF7	R&D system	Cat #: 251-kg-010
Wat-3a	R&D system	Cat #: 5036-wn-010
FGF2	R&D system	Cat #: 233-FB-010
LDN193189	Tocris	Cat #: 1435934-00-1
T3	MilliporeSigma	Cat#: 64245
Y-27632	Cell signaling technology	Cat #: 877-678-tech
EGF	R&D system	Cat #: 236-EG-200
Retinoic acid	Millipore sigma	Cat #: R2625-1G
DAPT	Sigma-Aldrich	Cat #: D5942
Heparin	Sigma-Aldrich	Cat #: H3149-500KU-9
FCCP	MedChemExpress	Cat #: HY-100410
Oligomycin	MedChemExpress	Cat #: HY-N6782
Rotenone	MedChemExpress	Cat #: HY-B1756
D-Glucose	Gibco	Cat #: 15023021
D-Luciferin potassium	Meilunbio	Cat#: MB1834-2
A83-01	Tocris	Cat #: 909910-43-6
Zinc sulfate	Sigma-Aldrich	Cat #: 83265-250ML-F
DAPI	Beyotime Biotechnology	Cat #: C1005
TrypLE Express	Life Technologies	Cat #: 12605
Triton X-100	Sigma-Aldrich	Cat #: T8797
Streptozotocin	Sigma-Aldrich	Cat #a18883-66-4
Paraformaldehyde	Beyotime Biotechnology	Cat #: P0099
Penicillin/streptomycin	Gibco	Cat #: 15140122
NaOH	Sigma-Aldrich	Cat #:1310-73-2
NaCl	Sigma-Aldrich	Cat #:7647-14-5
Citric acid	Sigma-Aldirch	Cat#:77-92-9
Bovine serum albumin	Sigma-Aldrich	Cat#: 9048-4-8
NaHCO3	Sigma-Aldrich	Cat #:144-55-8
Fetal bovine serum	Hyclone	Cat #:SH30071.03
SDS	Merck	Cat #: 151-21-3
$\alpha 2\beta 1$ Integrin Ligand Peptide TFA	MedChemExpress	Cat #: HY-P1868A
Collagenase type I	Sigma-Aldrich	Cat #: 9001-12-1
Collagen I	HARVEYBIO	Cat #: 9007-34-5
Collagen VI	Rockland	Cat #:48781
Collagen IV	Sigma-Aldrich	Cat #: 9007-34-5
Laminin	APExBIO	Cat #: A1023-1
Hematoxylin & Eosin	Beyotime Biotechnology	Cat #: C0105M
Isoflurane	RWD Life Science	Cat #: R510-22-10
Collagenase P	Roche	Cat #: 71496523

(*Continued on next page*)

Continued		
REAGENT or RESOURCE	SOURCE	IDENTIFIER
Tolbutamide	MedChemExpress	Cat #: HY-B0401
Diazoxide	MedChemExpress	Cat #: HY-B1140
KCl	Macklin	Cat #: P816355
Dithizone	Sigma-Aldrich	Cat #: D5130
Trypsin 0.25%EDTA	Gibco	Cat #: C25200056
Critical commercial assays		
TUNEL SYSTEM	Roche	Cat #:121567910
Human C-peptide ELISA kit	ELK Biotechnology	Cat #: ELK8871
Human Insulin ELISA kit	ELK Biotechnology	Cat #: ELK4963
Human Glucagon ELISA kit	ELK Biotechnology	Cat #: ELK1081
DNA Tissue Kit	QIAGEN	Cat #: 51404
BCA	Beyotime Biotechnology	Cat #: P0009
CellTiter-Glo® 3D Viability Assay	Promega	Cat #: G9681
Live & Dead™ Viability/Cytotoxicity Assay	US Everbright	Cat #: L6037L
Deposited data		
dAM and dpECM	ProteomeXchangeConsortium	PXD047565
Experimental models: Cell lines		
Human iPSC	Beijing Saibei Biotechnology	N/A
Experimental models: Organisms/strains		
NOD/SCID mice	Gem Pharmatech	N/A
C57BL/6	Gem Pharmatech	N/A
Software and algorithms		
FlowJO	https://www.flowjo.com	Version 10
GraphPad Prism	https://www.graphpad.com/scientific-software/prism/	Version 8
ImageJ	https://imagej.nih.gov/ij/	Version2.0.0-rc-69/1.52p
Other		
DMEM/F12 media	Gibco	Cat #: 11320033
MTeSR1	Stem cell Technologies	Cat #: 85850
PBS-Mg-Ca	Gibco	Cat #:14190-250
PBS+Mg+Ca	Gibco	Cat #:14040-182
RPMI	Corning	Cat #: 25-055-CM
CMRL	Corning	Cat #: 15-110-CV
Cell culture-grade water	Gibco	Cat #: A1287303
Bovine serum albumin	Proliant biologicals	Cat# 68700
Krbs buffer	Sigma-Aldrich	Cat #: K3753
LSM900	ZEISS	N/A
Seahorse Xfe-24	Agilent	N/A
FACSymphony S6	BD	N/A
Thunder Imager 3D Live Cell	Leica	N/A
Luznoche® B	SpectralMagic	N/A
Glucometer	Johnson	N/A
Dynamic universal testing machine	Bose	N/A
Cell countess 3	Invitrogen	N/A

EXPERIMENTAL MODEL AND STUDY PARTICIPANT DETAILS

Animals

Male NOD/SCID mice and C57BL/6, aged 4-6 weeks, were purchased from Gem Pharmatech Co., Ltd. These animals were housed in a specific pathogen-free animal facility that strictly adhered to a 12-h light/dark cycle. For experimental consistency, all

experiments involving animals utilized mice that were matched in terms of sex, age, and background. All animal procedures were according to the law and institutional guidelines approved by the Ethics Committee of Guangdong Provincial People's Hospital.

Decellularized amniotic membrane

The use of human Amniotic membrane (AM) was approved by the Institutional Ethics Committee of Guangdong Provincial People's Hospital. Human placental tissue was collected from healthy women who underwent cesarean deliveries. The AM was mechanically separated from the chorions of the placentas and subsequently rinsed with cold phosphate-buffered saline (PBS) to remove any resident blood stains. Subsequently, the AM was sectioned into approximately 2 cm^2 pieces. These pieces underwent decellularization immersed in 5% SDS solutions with gentle agitation for 2h. Following this, the pieces were subjected to a 0.1% Triton X-100-PBS buffer treatment for 12h whilst maintained at 4°C. Finally, they were rinsed with ultrapure water for 30 minutes. The decellularized outcome was authenticated using hematoxylin and eosin (H&E) stain and DNA content assays.

In this study, decellularized AM (dAM) served a bifunctional purpose. Initially, dAM underwent lyophilization, was ground into powder under liquid nitrogen, and then stored at -80°C for future use. This allowed for the preparation of hydrogels with various blends of basement membrane extract (BME2)/dAM, aiding in the differentiation of hiPSC spheroids. Secondly, dAM was utilized to support the development and engraftment of islet organoid patches, providing a structural matrix conducive to tissue formation.

Human islets

Human pancreatic islet tissue was obtained from the Guangdong Provincial People's Hospital or the First Affiliated Hospital of Guangzhou Medical University. The use of human islets complied with both legal and institutional guidelines approved by the Ethics Committee of Guangdong Provincial People's Hospital. All islets were isolated with the consent and intended for research or clinical transplantation. Islets were utilized, isolated using collagenase P-induced enzymatic digestion, and subsequently purified by hand picking. The isolated islets were cultivated in 10% FBS-CMRL1066 medium at 37°C with 5% CO_2 for further experiments.

METHOD DETAILS

Cell culture and cell differentiation

The human iPSC employed in this study was acquired from Beijing Saibei Biotechnology Company. These undifferentiated hiPSCs were maintained on tissue culture polystyrene (TCP) plates, which were coated with Matrigel, within a mTeSR1 medium environment. Once the cell confluence reached 70-90%, cells were passaged using EDTA. For differentiation experiments, hiPSCs were dissociated employing TrypLE Express and carefully plated onto ultralow attachment round bottom microwell plates at a density of 1000-3000 cells per well to promote aggregate formation over a 2-day duration.

Following this, hiPSCs spheroids were embedded within BME2/dAM ECM hydrogel and subjected to a sequential differentiation regimen to yield islet organoids. The differentiation protocol comprises five stages. Detailed descriptions of the growth factors and small molecules used are furnished in the preceding table. The basal medium employed for the experiment was enriched with a 1% supplemented of N2 and N21 in the RPMI medium. The medium's composition underwent alterations at every stage, detailed as follows:

Stage 1 (3 days): Basal medium supplement with 100 ng/ml Activin A, 3 μM CHIR99021, and 25 ng/ml wnt-3a;

Stage 2 (2 days): Basal medium supplement with 50 ng/ml KGF and 50 ng/ml FGF2;

Stage 3 (2 days): Basal medium supplement with 50 ng/ml Noggin, 2 μM LDN193189, 2 μM Retinoic acid;

Stage 4 (5 days): Basal medium supplement with 2 μM Retinoic acid &10 μM Nicotanimide & 5 mg/ml Vitamin C & 50 ng/ml EGF & 25 ng/ml KGF;

Stage 5 (10 days): Basal medium supplement with 1 μM DAPT, 10 μg/ml Heparin, 1 μM 3,3',5'-Triiodo-L-thyronine& 20 mM Glucose, 10 μM A83-01, 50 ng/ml Insulin-like growth factor, 2 μM Zinc sulfate, and 50 ng/ml exendin 4.

Karyotype analysis

Karyotype analysis was conducted on human iPSC using standard protocols for high-resolution G-banding (400G–500G). Chromosomal integrity, including numerical and structural aspects, was assessed utilizing CytoVision software (Leica Biosystems).

Viability assessment

The viability of cells was determined via staining with a live/dead viability/cytotoxicity kit from Life Technologies as per the manufacturer's instructions. Cells were incubated with 2 μM Calcein AM and 4.5 μM propidium iodide (PI)-PBS solution for 30 minutes at 37°C. Post incubation, the cells were subjected to dual washes in PBS before fluorescence-based viability assessment using a Leica Thunder Imager 3D Live Cell microscope. Additionally, to evaluate the cytoprotective effects and functional maintenance of islet cells by dAM sheet or Col VI under ischemic stress, hiPSC-derived islet organoids were cultured under hypoxic conditions (1% oxygen and 5% CO_2 at 37°C) for 16 hours, following the manufacturer's instructions.

ATP measurement

The metabolic activity indicative of islet organoid viability was quantified using the CellTiter-Glo® 3D Cell Viability Assay (Promega, G9681). Sample islet organoids were dispensed into an opaque 96-well plate and incubated with 100 μl of the CellTiter-Glo® 3D

Reagent. Agitation of the well contents was gently performed for 5 minutes to instigate cell lysis, followed by a 2-minute stabilization period to ensure complete cell lysis before luminescence measurement.

Western blotting

Samples collection was performed in a RIPA buffer, which contained a 1× protease and phosphatase inhibitor, under chilled conditions. The lysates were processed via homogenization, subjected to sonication for 10 seconds, and then centrifuged at 12,000 rpm for 10 minutes at 4°C to remove cellular debris. Protein concentrations were determined utilizing a BCA assay kit. The proteins were subsequently loaded onto sodium dodecyl sulfate-polyacrylamide gel electrophoresis, followed by transfer to PVDF membranes. The membranes underwent a blocking step with 5% silk milk for 1 hour at room temperature (RT). These membranes were subsequently incubated overnight at 4°C with primary antibodies (as listed above table), and the detection was carried out using an enhanced chemiluminescence HRP substrate.

Histology and immunostaining

Differentiated cell clusters, native tissues, and retrieved grafted tissues underwent fixation using 4% paraformaldehyde (PFA) for 2 hours at RT or overnight at 4°C. Following fixation, the samples were embedded in paraffin and sectioned into slices of 5-8 μm in thickness. These slides subsequently underwent dewaxing and rehydration processes. Hematoxylin and eosin staining were carried out for nuclear and cytoplasmic visualization, with durations of six and three minutes, respectively. For immunofluorescence analyses, we conducted heat-induced antigen retrieval. These slides were then washed with PBS and received a blocking with 5% donkey serum-Triton X-100 for 1h at RT. Subsequently, slides were subjected to incubation with primary antibodies (as listed in the preceding table) overnight at 4°C. The secondary antibodies, diluted similarly, were incubated for 1 hour at RT. Following this, the slides were stained with DAPI, rinsed with PBS, covered with coverslips, and sealed with nail polish. Representative regions of the slides were captured using either ZEISS or LEICA microscope.

Ex vivo static and dynamic glucose-stimulated insulin secretion (GSIS)

For static insulin secretion assay, uniform-sized islet organoids were selected and incubated in Krebs-Ringer buffer (KRB) for 30 minutes. The organoids were sequentially exposed to KRB containing 2 mM glucose for 1 hour, followed by 20 mM glucose for an additional hour. Supernatants were collected after each exposure. Subsequently, the organoids were subjected to KRB with 2 mM glucose and 30 mM KCl (a depolarization challenge) for 1 hour, after which the supernatant was collected again. Cell counts were determined using an Automated Cell Counter, and human insulin or C-peptide levels in the supernatants were measured using an ELISA kit.

For dynamic insulin secretion assays, equal numbers of hiPSC-derived islets or human islets were divided into chambers and processed using a fully automated Perifusion System (BioRep) The chambers were perfused at a flow rate of 0.25 ml/min with KRB, with sampling every 4 minutes. Perifused islets were equilibrated in 2 mM glucose for 90 minutes before starting experimental protocols involving low (2 mM) and high (20 mM) glucose, and 30 mM KCl perfusions. Flowthrough samples were collected throughout the experiment, and insulin or C-peptide levels were measured using an ELISA kit. After the experiment, insulin and DNA content from the hiPSC-derived islet clusters or human islets were measured using acid-ethanol extraction and a DNA Assay Kit, respectively.

Enzyme-linked immunosorbent assay (ELISA)

Quantitative assessments of human insulin, C-peptide, and glucagon were obtained using specific ELISA kits (insulin: ELK4963, C-peptide: ELK8871, glucagon: ELK1081; ELK Biotechnology). All procedures followed the manufacturer's instructions precisely, with analyses performed in triplicate for each sample.

Calcium imaging

Calcium imaging protocol was adapted from Balboa et al. previous study.[4] Briefly, hiPSC-derived islet clusters and human islets were washed in KRB solution at 37°C for 15 minutes. After washing, the islets were adhered to poly-l-lysine-coated coverslips in a 50 μl chamber on the stage of a Zeiss LSM 900 and superfused with buffer at a rate of 160 μl/min. The chamber holder and ×40 objective were maintained at 37°C by custom-built thermostats. The testing procedure involved sequential exposure to 2 mM glucose, 250 μM diazoxide, 1 mM Tolbutamide, and 30 mM KCl. Fluo4-AM dye, in combination with Ca^{2+}, produced high-resolution time-series images with strong fluorescence. Images were captured every 2 seconds using a Zeiss LSM 900 at an excitation/emission wavelength of 488/525 nm. Intracellular Ca^{2+} levels $[Ca^{2+}]_i$ were calculated from the background-corrected Fluo 4-AM 488nm/525nm fluorescence excitation ratio within manually defined cell-sized regions of interest. Data are presented as example traces or heatmaps from individual islet clusters and cells, as well as histograms showing the changes in $[Ca^{2+}]_i$ under various conditions. For comparison, the response to each treatment was calculated as the difference in time-averaged $[Ca^{2+}]_i$ from the preceding condition, normalized to $[Ca^{2+}]_i$ at 2 mM glucose. Quantitative analyses of image series and fluorescence intensity were conducted using Image J/FIJI and GraphPad Prism software.

Flow cytometry

For flow cytometry analysis, we acquired a single-cell suspension using TrypLE Express dissociation, followed by a 30-minute fixation in 4% PFA. Subsequently, the cells were twice washed with ice-cold PBS and permeabilized using 0.1% Triton X-100-PBS for

1 hour. Next, we incubated them with 5% donkey serum-blocked buffer. The cells were incubated with primary antibodies or isotypes and kept on ice overnight. Following the incubation with either Alexa Fluor 488-conjugated or Alexa Fluor 594-conjugated secondary antibodies for 2 hours at 4°C. Afterward, the cells were rinsed with PBS, resuspended in ice-cold PBS, and analyzed on a flow cytometer. Data processing and interpretation were carried out employing FlowJo v10 software.

Mitochondrial respiration measurement

Mitochondrial respiration was quantified using the Seahorse XF-24 Metabolic Flux Analyzer (Seahorse Bioscience). hiPSC-derived islet organoids and human islets were aliquoted and seeded onto an XFe-24 microplate a day before the Seahorse assay. Microplates were incubated at 37°C in basal Seahorse XF medium containing 2 mM glucose in a CO_2-free environment for 1 hour before measurement. All protocols were conducted at a constant temperature of 37°C in real-time throughout the assay. After measuring basal respiration, a sequential inject of 2 mM glucose, 20 mM glucose, 5 μM oligomycin (an ATP synthase inhibitor), 1 μM carbonyl cyanide-4 (trifluoromethoxy) phenylhydrazone (FCCP, a mitochondrial uncoupling agent), and 5 μM rotenone/antimycin A (inhibitors of electron transport chain complexes I and III) was performed in basal Seahorse XF medium. Respiration rates were normalized to the basal OCR before the addition of nutrients or small molecules. Insulin and DNA content of each well was determined using an ELISA kit and DNA Assay Kit, respectively.

Transmission electron microscopy

Samples of the hiPSC-islet clusters, hiPSC-islet grafts, human islet grafts, and AM tissue were initially rinsed with PBS, then chemically fixed with 3% glutaraldehyde in a sodium cacodylate buffer (pH 7.4). Following triple washed with sodium cacodylate buffer, the specimens were post-fixed in 1% osmium tetroxide with 0.1% sodium cacodylate for 1 hour. The specimens were subsequently dehydrated and embedded in Epon (TAAB 812). Using a diamond knife, the samples were sectioned at a thickness of 70 nm perpendicular to the substrate. Ultrathin sections were collected on 200 mesh copper grids. The sections were initially stained with a 4% uranyl acetate solution for 15 minutes, then stained with a 4% uranyl acetate solution for an additional 10 minutes, and finally stained with lead citrate for 7 minutes. Micrographs were captured with a Hitachi HT7800 microscope, equipped with a Rio9 CMOS camera, operated at 100 kV. The images were processed and analyzed utilizing the Image J software program.

Scanning electron microscopy

Cell cluster and AM samples were subjected to fixation with 2.5% glutaraldehyde for 2 hours at RT. Subsequently, the samples underwent a stepwise dehydration process employing a sequence of ethanol solutions with concentrations escalating from 50% to 100%. The samples were thereafter air-dried in a sterilized environment for 1 hour and were subsequently subjected to sputter-coated with a thin layer of palladium-gold alloy. Lastly, the prepared samples were subjected to observation under a Scanning Electron Microscope manufactured by Hitachi.

TUNEL staining

The assessment of apoptotic cells was performed utilizing the terminal deoxynucleotidyl transferase (TdT) mediated dUTP nick end-labeling (TUNEL) assay (Roche, Mannheim, Germany), according to manufacturer's guidelines. In brief, slides were subjected to a dual PBS wash and subsequently incubated with 100 μl of TUNEL reagent for one hour at room temperature. Thereafter, the stained specimens were immersed in a PBS bath, before subsequent application of DAPI staining. Observation of these preparations was then undertaken via a LEICA microscope.

Cryopreservation and recovery of hiPSC-islet organoids

For cryopreservation, we prepared the dAM sheet-bound islet organoids in a cryoprotective medium composed of 40% fetal bovine serum (FBS), 10% dimethyl sulfoxide (DMSO), and 50% final stage medium with 10 μM/mL Y27632. Following immediate transfer into a cell freezing receptacle, the samples were subjected to freezing at -80°C for 24 hours. Thereafter, for long-term storage, the vials were transferred to liquid nitrogen. During the recovery process, the cryopreserved vials were thawed in a 37°C water bath before the islet organoids attached to the dAM sheet were rinsed with RPMI basic medium. The organoids were cultured in RPMI basic medium with 1% B27 supplement. Viability and yield post-recovery were evaluated through live/dead staining assay.

Glucolipotoxicity

To validate the effect of Col VI in safeguarding islet organoids against cellular death, we conducted a glucolipotoxicity test on the cluster of islets. Briefly, the islet organoids were subject to 20 mM glucose and 1 μM lipid conditions for 1 hour and then stained with a live/dead assay.

Subcutaneous transplantation

Immunodeficient male mice of the same age were subjected to a 12-hour fasting before the procedure. After which, we intraperitoneally injected a freshly prepared solution of citrate acid/sodium citrate streptozotocin (STZ), dose at 150 mg/kg. Only the mice exhibiting blood glucose levels surpassing 16.7 mmol/ml during non-fasting periods for successive days were selected as candidates for diabetes-oriented transplantation. Under isoflurane anesthesia, a small skin incision of approximately 0.5 cm in length was made on the dorsal midline of each mouse, thereby creating a subcutaneous pocket for the insertion of islet organoids. Subsequently, the

incision was sutured closed. We monitored the recipient mice's non-fasting blood glucose levels and body weight daily and took blood samples from the tail vein for blood glucose measurement. At 3 months post-transplantation, the mice were euthanized, and the grafts were harvested for subsequent immunohistochemistry analysis.

Intraperitoneal glucose tolerance test (IPGTT)

Mice recipients at post-transplantation months 1 and 3 were subjected to overnight fasting prior to intraperitoneal injection of D-glucose at a dosage of 2 g/kg. Subsequently, we monitored blood glucose levels at regular intervals of 30 minutes, for a total duration of 120 minutes. Using a human insulin/C-peptide ELISA kit, we measured the concentrations of serum human insulin and C-peptide in all blood samples at both 0 and 30 minutes post-glucose injection.

Bioluminescence monitoring of transplanted islet organoids

For subcutaneous transplantation, islet organoids were genetically modified to consistently express luciferase via lentiviral-mediated gene transfer. The survival of islet organoids within the recipient's subcutaneous tissue was visualized through the intraperitoneal injection of 100 μl D-luciferase (20 mg/ml). The Luznoche® B imaging system (SpectralMagic) was used to capture images of mice, allowing for the observation of the in vivo distribution of islet organoids.

High performance liquid chromatography-tandem mass spectrometry (HPLC-MS/MS)

Samples of dAM and mouse pancreatic decellularized scaffolds were digested by the Filter-aided sample preparation (FASP). Briefly, samples were chopped and lyophilized, and then homogenized in urea lysis buffer (8 M sequencing grade urea, 100 mM Tris-HCl, PH 8.0) and transferred to an ultrafiltration tube (Ultracel-10K, Millipore, USA). Then reduced with a 5 mM dithiothreitol (DTT) for 30 min at 56°C, and then alkylated with 11 mM iodoacetamide (IAA) for 15 min at RT in the dark as described elsewhere. Subsequently, the samples underwent digestion with Trypsin (at a ratio of 1:50, W/W, V5111, Promega, USA). After desalted by C18 column, purified peptides were separated on nanoElute UHPLC system (Bruker Daltonics). followed detect by using timsTOF Pro (Bruker Daltonics) mass spectrometer. The resulting MS/MS data were processed using MaxQuant search engine (v.1.6.15.0). Tandem mass spectra were searched against the human/mouse SwissProt database concatenated with reverse decoy database. Trypsin/P was specified as cleavage enzyme allowing up to 2 missing cleavages. The mass tolerance for precursor ions was set as 20 ppm in the first search and 5 ppm in main search, and the mass tolerance for fragment ions was set as 0.02 Da. Carbamidomethyl on Cys was specified as fixed modification, and acetylation on protein N-terminal and oxidation on Met were specified as variable modifications. FDR was adjusted to < 1%.

Engineering biomimetic ECM scaffold for islet organoids

We prepared a solution containing 4 mg/ml Collagen I, 4 mg/ml Collagen IV, 4 mg/ml Collagen VI, and 1 mg/ml Laminin to fabricate an ECM scaffold for islet organoids. Under sterile conditions, the mixture was diluted using 10× Dulbecco's Modified Eagle Medium (DMEM). Using 1N NaOH, the pH of the mixture was promptly neutralized to 7.4. Subsequently, the intermixed solutions were aliquoted into cylindrical molds within syringes, followed by incubation at 37°C for 1 hour to initiate gelation. Post-gelation, the formed scaffold seeds were carefully transferred from the syringe molds onto the culture plate, followed by the addition of the appropriate culture medium. The fabrication process did not involve the use of any crosslinking agents.

Mechanical properties

The universal electronic testing machine was employed to assess the hydrogel's mechanical properties. The cylindrical hydrogel specimens were positioned centrally on the horizontal measuring platform. The mechanical properties of the hydrogel were evaluated using an electronic universal testing machine. Cylindrical hydrogel samples were prepared and placed at the center of the horizontal measuring platform. A loading force of 100N was applied to the hydrogel at 10mm/min, and the data was recorded continuously until a deformation rate of 50% was achieved.

Dithizone staining

Dithizone selectively stains zinc granules within beta cells red, making it useful for identifying isolated and re-aggregated human islets. Fresh islets were enzymatically dissociated from native tissue, and re-aggregated islet samples were treated with 5 mg/ml DTZ-DMSO buffer for 5 minutes at room temperature. The samples were then supplemented with CMRL1066 medium for imaging.

QUANTIFICATION AND STATISTICAL ANALYSIS

All statistical analyses were performed using GraphPad software. Values were presented as mean or median based on their distribution. Statistical differences were determined by two-tailed Student's t-test, a one-way ANOVA coupled with a Dunnett test for multiple comparisons, or two-way ANOVA coupled with Tukey's test for multiple comparisons. The significance levels were denoted as ns, *, **, and ***, corresponding to non-significance and p-values less than 0.05, 0.01, and 0.001, respectively.